

**CHARACTERIZATION OF IMPACT INITIATION OF  
ALUMINUM-BASED INTERMETALLIC-FORMING REACTIVE  
MATERIALS**

A Thesis  
Presented to  
The Academic Faculty

by

Michael D. Tucker

In Partial Fulfillment  
of the Requirements for the Degree  
Master of Science in Mechanical Engineering in the  
School of Mechanical Engineering

Georgia Institute of Technology  
December 2011

Report Documentation Page			Form Approved OMB No. 0704-0188		
Public reporting burden for the collection of information is estimated to average 1 hour per response, including the time for reviewing instructions, searching existing data sources, gathering and maintaining the data needed, and completing and reviewing the collection of information. Send comments regarding this burden estimate or any other aspect of this collection of information, including suggestions for reducing this burden, to Washington Headquarters Services, Directorate for Information Operations and Reports, 1215 Jefferson Davis Highway, Suite 1204, Arlington VA 22202-4302. Respondents should be aware that notwithstanding any other provision of law, no person shall be subject to a penalty for failing to comply with a collection of information if it does not display a currently valid OMB control number.					
1. REPORT DATE <b>DEC 2011</b>		2. REPORT TYPE		3. DATES COVERED <b>00-00-2011 to 00-00-2011</b>	
4. TITLE AND SUBTITLE <b>Characterization Of Impact Initiation Of Aluminum-Based Intermetallic-Forming Reactive Materials</b>				5a. CONTRACT NUMBER	
				5b. GRANT NUMBER	
				5c. PROGRAM ELEMENT NUMBER	
6. AUTHOR(S)				5d. PROJECT NUMBER	
				5e. TASK NUMBER	
				5f. WORK UNIT NUMBER	
7. PERFORMING ORGANIZATION NAME(S) AND ADDRESS(ES) <b>Georgia Institute of Technology, Georgia, GA, 30332</b>				8. PERFORMING ORGANIZATION REPORT NUMBER	
9. SPONSORING/MONITORING AGENCY NAME(S) AND ADDRESS(ES)				10. SPONSOR/MONITOR'S ACRONYM(S)	
				11. SPONSOR/MONITOR'S REPORT NUMBER(S)	
12. DISTRIBUTION/AVAILABILITY STATEMENT <b>Approved for public release; distribution unlimited</b>					
13. SUPPLEMENTARY NOTES					
14. ABSTRACT <b>The objective of this work is to evaluate the reaction initiation characteristics of quasi-statically compressed intermetallic-forming aluminum-based reactive materials upon impact initiation, consisting of equi-volumetric tantalum-aluminum, tungsten-aluminum nickel-aluminum, and pure aluminum. A modified Taylor rod-on-anvil setup was employed to determine the reaction initiation threshold kinetic energy and actual energy for plastic deformation and subsequent reaction. Experimental sample remnants were recovered and examined through X-ray diffraction to determine reaction products.</b>					
15. SUBJECT TERMS					
16. SECURITY CLASSIFICATION OF:			17. LIMITATION OF ABSTRACT <b>Same as Report (SAR)</b>	18. NUMBER OF PAGES <b>85</b>	19a. NAME OF RESPONSIBLE PERSON
a. REPORT <b>unclassified</b>	b. ABSTRACT <b>unclassified</b>	c. THIS PAGE <b>unclassified</b>			

**CHARACTERIZATION OF IMPACT INITIATION OF  
ALUMINUM-BASED INTERMETALLIC-FORMING REACTIVE  
MATERIALS**

Approved by:

Dr. Naresh Thadhani, Advisor  
School of Mechanical Engineering  
*Georgia Institute of Technology*

Dr. Joe Cochran  
School of Mechanical Engineering  
*Georgia Institute of Technology*

Dr. Antonia Antoniou  
School of Mechanical Engineering  
*Georgia Institute of Technology*

Dr. Ken Gall  
School of Mechanical Engineering  
*Georgia Institute of Technology*

Date Approved: August 2011

*To all those who made a sacrifice of time, money, thoughts, prayers, and patience for me,  
and others like me. May I be a blessing to others as others have been to me and before me  
for all those after.*

*To my family who I would do anything for, my parents, and to the memory of Uncle  
Willie and Uncle Lewis whom my family lost this year, and to my great-grandfather and  
greatest inspiration, Roy Nathaniel Tucker....*

*Papa, "I ain't dead yet"*

## ACKNOWLEDGEMENTS

First I would like to give honor to my Lord and Savior Jesus Christ for all the blessings that have been bestowed upon me, including the opportunity to further my education. I want to thank Dr. Thadhani for extending the opportunity to work and learn in his lab. I would like to thank my parents for their constant support of all my endeavors in life and for pushing me to be the man that I am today. I want to thank the Black Graduate Student Association for providing a home away from home, academic and social support, friendships that I will never forget, mentorship, helping me to discover more about myself, and the experience to give back a portion of what I was given in the capacity of your Vice-President for the 2010-11 academic year. I would like to thank Dr. Gary May for his constant support of my academic career and both he and Dr. Leyla Conrad for allowing me the opportunity to be a part of the SURE program as both a student in 2008 and as a coordinator this Summer 2011 year.

My lab mates have been key in my survival. Thank you for being there for my constant badgering of questions and random conversations, this degree would not be possible without you. I would like to thank Anna Alexander for her work in running XRD on my samples, Sean Dixon for his unfathomable ethic in testing and support in the impact experiments, Brad White and Christopher Neel for their instruction on how to operate the “little” gun, Greg Kennedy, Brady Aydelotte, Paul Specht, and Sean Kelly for constantly fielding my questions and providing perspective, and I especially thank Chris Weherenburg for his help in XRD/Glove Box/Sample preparation, providing a helping hand in experimentation, repeatedly taking time out to tend to matters less pressing to him, helping with analysis, and for his mentorship. He is a true and genuine person and I wish him and the entire lab all the best in their future endeavors. I also acknowledge the work of Dr. Seiwei Du that provided the foundation for my research.

There are a host of reasons as to why I am able to say these words today and I am

extremely thankful for all the love, appreciation, care, long nights, points of confusion, moments of clarity, and comradery that I have experienced in my stay. Each and every experience no matter how daunting or pleasant has been beneficial to me in some way shape or form and I hope I can give back some of what was given to me to those who come after. The funding for this research was provided by ONR/MURI Grant No. N000147-07-1-0740.

## TABLE OF CONTENTS

<b>DEDICATION</b> . . . . .	<b>iii</b>
<b>ACKNOWLEDGEMENTS</b> . . . . .	<b>iv</b>
<b>LIST OF TABLES</b> . . . . .	<b>viii</b>
<b>LIST OF FIGURES</b> . . . . .	<b>ix</b>
<b>SUMMARY</b> . . . . .	<b>xii</b>
<b>I INTRODUCTION</b> . . . . .	<b>1</b>
<b>II BACKGROUND</b> . . . . .	<b>3</b>
2.1 Reactive/Energetic Material Characteristics . . . . .	3
2.2 Thermal Initiation . . . . .	5
2.2.1 Electrical Ignition . . . . .	6
2.2.2 Filament Ignition . . . . .	7
2.2.3 Differential Scanning Calorimetry and Differential Thermal Analysis . . . . .	9
2.2.4 Laser Ignition . . . . .	11
2.3 Impact Initiation . . . . .	13
2.3.1 Drop Weight Test Setup . . . . .	13
2.3.2 Mechanical Lever Impact Initiation . . . . .	17
2.3.3 Taylor Rod-on-anvil Impact Test . . . . .	18
2.3.4 Dynamic Energy Release Characterization using Pig Test . . . . .	21
2.3.5 Shock Compression of Reactive Powder Mixtures . . . . .	25
2.4 Background Conclusions . . . . .	28
<b>III EXPERIMENTAL PROCEDURE</b> . . . . .	<b>30</b>
3.1 Objectives and Approach . . . . .	30
3.2 Reactive Materials Systems . . . . .	30
3.3 Sample Mixing and Compaction . . . . .	34
3.4 Modified-Taylor Rod-on-Anvil Impact Test Setup . . . . .	34
3.5 Reaction Product Recovery and Characterization . . . . .	37

<b>IV RESULTS AND DISCUSSION . . . . .</b>	<b>40</b>
4.1 Intermetallic Systems Overview of Results . . . . .	40
4.2 Comparison of Reaction Initiation Energy Thresholds . . . . .	53
4.2.1 Effect of Environment: Air Versus Vacuum . . . . .	53
4.2.2 Material System Density Effects . . . . .	53
4.2.3 Particle Size Effects . . . . .	55
4.2.4 Material System Strength Effects . . . . .	56
4.3 Recovery Experiments and Characterization . . . . .	57
4.3.1 Polycarbonate Ring Experimental Results . . . . .	57
4.3.2 Recessed Projectile Experimental Results . . . . .	61
<b>V CONCLUSIONS AND FUTURE WORK . . . . .</b>	<b>64</b>
5.1 Concluding Remarks . . . . .	64
5.2 Recommendations for Future Work . . . . .	65
5.2.1 Characterization Techniques . . . . .	65
5.2.2 Material Systems . . . . .	66



## LIST OF TABLES

1	Heats of Reaction of various thermite mixtures . . . . .	5
2	Heats of Reaction of various intermetallic forming compounds . . . . .	5
3	Heats of Reaction of combustions of various metals . . . . .	5
4	Table of relevant Al, Ni, Ta, and W properties . . . . .	31
5	Material systems mass ratios for selected stoichiometries . . . . .	31
6	Material systems volume fraction for selected stoichiometries . . . . .	32
7	Material systems densities for selected stoichiometries . . . . .	32
8	Sample data of Al experiments and results; part (a) denotes air experiments and part (b) represents vacuum experiments, all with no reaction . . . . .	41
9	Sample data of Ni+Al experiments and results; part (a) denotes air experiments and part (b) represents vacuum experiments . . . . .	42
10	Sample data of Ta+Al experiments and results; part (a) denotes air experiments and part (b) represents vacuum experiments . . . . .	43
11	Sample data of W+Al experiments and results; part (a) denotes air experiments and part (b) represents vacuum experiments . . . . .	44
12	Lowest threshold conditions for reaction initiation for each intermetallic system in (a) air and (b) vacuum for a nominal density of 94 - 97 percent TMD . . . . .	49
13	Lowest Values for each equi-volumetric system of experimentally recorded velocity, velocity determined at reaction, and horizontal and vertical range and tolerances per pixel and calculated actual initiation energy Eq.3 , energy dissipated in reaction Eq. 2, actual specific kinetic energy Eq. 4, and energy density Eq. 5 and minimum and maximum actual kinetic energy determined from pixel ranges at reaction per system . . . . .	53

## LIST OF FIGURES

1	Cross-sectional geometry of electrical ignition setup . . . . .	6
2	Experimental and computational results of ignition current plotted as a function of contact radius experimental results . . . . .	7
3	Filament Ignition Experimental Setup . . . . .	8
4	Photodiode trace showing spike in temperature . . . . .	8
5	Differential Scanning Calorimetry traces obtained for $\text{Li}_x\text{NiO}_2$ plus electrolyte	10
6	Baseline-corrected Differential Scanning Calorimetry traces collected for nanocomposite powder with bulk composition $\text{Al-MoO}_3$ . . . . .	10
7	Electrodynamic levitator . . . . .	11
8	Electrodynamic levitator setup . . . . .	11
9	Record of the light emission during the burning phase of spherical Mg particles	12
10	Ignition probability of spherical Mg particles . . . . .	12
11	Drop Weight experimentation thermite compositions . . . . .	13
12	Drop Weight Schematic . . . . .	14
13	Pre-sheared Drop Weight experiment setup . . . . .	14
14	Inclined Drop Weight schematic . . . . .	14
15	Deformation versus time curves for right-circular and pre-sheared thermite disks . . . . .	16
16	Geometry of mechanical lever impact setup . . . . .	17
17	Results of mechanical lever-arm impact tests . . . . .	17
18	Examples of post-Taylor-test 164-caliber specimens . . . . .	18
19	Dynamic stress estimates for the 164-caliber and 215-caliber Taylor rod-on-anvil test specimens . . . . .	19
20	Images of PTFE-Al samples shot in Taylor rod-on-anvil experiments . . . .	20
21	Shear-induced ignition in PTFE-Al Taylor rod-on-anvil test . . . . .	20
22	Pig-test schematic . . . . .	22
23	Pig-test experimental images . . . . .	23
24	Reaction efficiencies of various metal-polymer energetic materials . . . . .	24
25	Density effect in relative energy release of various energetic material systems	25
26	Parallel-plate impact experimental flier-target assembly . . . . .	26

27	Plot of shock velocity and input stress for the Ni-flake mixtures . . . . .	27
28	X-ray diffraction example trace of $\text{Ti}_5\text{Si}_3$ . . . . .	28
29	Schematic of 12-capsule Sawaoka shock recovery fixture . . . . .	28
30	SEM images showing the spherical morphologies of (a) Al and each of the constitutive mixtures (b) Ni+Al (c) Ta+Al and (d) W+Al . . . . .	33
31	Schematic and photograph of sample mounted on a projectile, Left being sample drawing and dimensions and the right being a top and side view of a finished projectile . . . . .	35
32	Schematic of experimental set up, with projectile, laser beam velocity trap, high-speed camera, and anvil . . . . .	36
33	Taylor rod-on-anvil impact initiation test in vacuum of Ta-Al equal-vol ratio at a speed of $\approx 500$ m/s . . . . .	36
34	Experimental setup with polycarbonate tube for debris capture . . . . .	38
35	Example of polycarbonate tube used in experimentation with "spray" ring of debris . . . . .	38
36	Diagram of the recessed round, all measurements are in millimeters . . . . .	39
37	Top (a) and side (b) views of filled recessed round . . . . .	39
38	Sample data of Al experiments and results; (a)denotes air and (b) represents vacuum. *Nanoparticle and 40 micron data points were provided from the work of Dr. Seiwei Du. . . . .	45
39	Sample data of Ni+Al experiments and results; (a)denotes air and (b) represents vacuum. . . . .	46
40	Sample data of Ta+Al experiments and results; (a)denotes air and (b) represents vacuum. . . . .	47
41	Sample data of W+Al experiments and results; (a)denotes air and (b) represents vacuum. . . . .	48
42	Graph of experimental data points by system plotted by the Kinetic Energy verses sample density in (a) air and (b) vacuum. . . . .	50
43	Kinetic energy of the Cu sabot(projectile) and pellet plotted as a function of percent theoretical maximum density for Ni+Al pellet . . . . .	55
44	Figure showing labeled points of percent TMD verses KE, for Ni-Al differing in particle sizes of -325 Mesh and +325 -200 mesh . . . . .	56
45	XRD trace of experimentally reacted Al fired at 476 m/s in air with at 99.7 percent TMD with no reaction products . . . . .	58
46	XRD trace of reacted equi-volume mix of Ni+Al at 469m/s in air at 92.4 percent TMD with no reaction products . . . . .	58

47	XRD trace of reacted equi-volume mix of Ta+Al at 474m/s in vacuum at 87.4 percent TMD with no reaction products . . . . .	59
48	XRD trace of reacted equi-volume mix of Ta+Al in air at 413m/s at 91.2 percent TMD with no reaction products . . . . .	59
49	XRD trace of reacted equi-volume mix of W+Al in vacuum at 478m/s at 94.1 percent TMD with no reaction products. The unidentified peaks at approximately 42 and 43 deg belong to Cu and possibly $\text{Al}_2\text{Cu}_3$ . . . . .	60
50	XRD trace of reacted equi-volume mix of W+Al in air at 465m/s at 93.3 percent TMD with no reaction products . . . . .	60
51	XRD trace of recessed projectile packed with pure Al fired at maximum velocity $\approx 480\text{m/s}$ in air . . . . .	62
52	XRD trace of recessed projectile packed with equi-volume mix of Ni+Al fired at maximum velocity $\approx 480\text{m/s}$ in air . . . . .	62
53	XRD trace of recessed projectile packed with equi-volume mix of W+Al fired at maximum velocity $\approx 480\text{m/s}$ in air . . . . .	63
54	XRD trace of material recovered from recessed projectile packed with equi-volume mix of Ta+Al fired at velocities of (a)357m/s and (b)483m/s in air showing intermetallic reaction products . . . . .	63

## SUMMARY

The objective of this work is to evaluate the reaction initiation characteristics of quasi-statically compressed intermetallic-forming aluminum-based reactive materials upon impact initiation, consisting of equi-volumetric tantalum-aluminum, tungsten-aluminum, nickel-aluminum, and pure aluminum. A modified Taylor rod-on-anvil setup was employed to determine the reaction initiation threshold kinetic energy and actual energy for plastic deformation and subsequent reaction. Experimental sample remnants were recovered and examined through X-ray diffraction to determine reaction products.

The intermetallic-forming materials were evaluated based on their experimentally determined reaction initiation kinetic energy threshold, as a function of density, particle size differences and environmental effects considering both air and vacuum. Multiple experiments were conducted using the 7.62 mm diameter gas gun, while measuring velocity (ranging approximately between 320 and 480 m/s) and recovering the products for subsequent X-ray diffraction analysis.

The overall results indicate that of the various intermetallic-forming systems investigated, Ta+Al was the most reactive and was the only system where any reaction products were retrieved. While all of the intermetallic systems reacted in air, only Ta+Al and W+Al reacted in vacuum environment suggesting differences in reaction mechanisms influencing the reactivity of intermetallic mixtures. Based on the threshold energy for onset of reaction it appears that the Ta-Al compacts show reaction conditions below those required for reaction of Al in air. This combined with the fact that Ta+Al compacts also react in vacuum implies that the Ta+Al undergoes anaerobic intermetallic reaction while the other systems react with the oxidation of Al. The effect of compact packing density on the kinetic energy threshold for reaction initiation were also evaluated. It was observed more densely packed Ta+Al and Ni+Al powder compacts react more easily than less densely packed samples. While the effect of packing density is not as obvious in the case of pure Al and W+Al

powder compacts. Finally, a particle size effect is seen on Ni+Al on samples of  $\leq 92\%$  density where coarser (+325 -200 mesh) equal-volumetric powder mixtures were observed to be more reactive than finer Ni+Al (-325 mesh).

# CHAPTER I

## INTRODUCTION

Intermetallic-forming reactive materials are a form of energetic materials that can release large amounts of exothermic energy upon ignition. However, unlike explosives which have high levels of sensitivity to ignition/detonation, the aforementioned intermetallic-forming reactive materials are unique in that their reactivity can be adjusted based on their packing density, volumetric distribution, particle size, and various other properties [1]. Reactive materials are also relatively stable until faced with extreme conditions or impact loading (i.e. excessive force/impact, shock). Upon impact loading, reaction initiation results in the release of energy in the form of a temperature increase which often manifests through light emission. Dense compacts of these reactive materials can also have desirable mechanical properties, making them useful as structural energetic materials because they share both structural (load bearing) and energetic (energy release) properties [2].

Reactive materials can be explosive in nature or be designed in order to give off heat or different colors of light. Mixtures of various constituents can produce high heats of reaction and metal-oxidation combustion that make them desirable for military munition casings and other applications [3]. Evaluation of these materials has been conducted through thermal, mechanical, impact, and shock compression for initiation to determine reaction characteristics like density effects, contact area, events leading to reaction and its mechanisms, energy release, reaction product analysis and recovery, and other properties. However, these studies do not attempt to identify the effects atmosphere, either operating solely in air or some inert environment/vacuum, or provide the necessarily high strain rates to cause reaction while maintaining observed reaction visibility coupled with *in-situ* diagnostics. This could mean the loss of optimum reaction characteristics, in the case where oxidation reactions are desired, which may occur during initiation but result in intermetallic reaction products remaining.

To investigate the reaction characteristics of the structural energetic materials, modified-Taylor rod-on-anvil impact tests are used. This allows uniaxial stress propagation to be applied to samples in order to create high radial deformation and employs strain rates upwards of  $10^5/s$  [4, 5, 6]. Reactions occurring from the impact, during densification and/or deformation of the powder mixture, are witnessed by capturing the reaction light emitted in the tests using a high speed camera. Recovery techniques and x-ray diffraction (XRD) analysis of recovered materials allow for the characterization of the reaction products for each of the reactive material systems.

The impact initiation of reactions in quasi-statically pressed compacts of “reactive materials” consisting of aluminum-based intermetallic-forming powder mixtures (metallic powders that form a solid state phase) is investigated. Mixtures of tungsten and aluminum, tantalum and aluminum, nickel and aluminum, and pure aluminum, are examined to determine the threshold level of impact energy necessary to initiate an intermetallic-forming reaction, as a function of material system, volumetric distribution of reactants, compact density, and environment (vacuum/air). In addition, an added goal was to identify the reaction products for the individual systems. The overall objective is to determine the occurrence of reaction due to combustion (oxidation) of Al, or as anaerobic intermetallic reaction between the reactants in the pressed powder compacts.

In this thesis, background information regarding reactive materials and their impact initiation characteristics described in the literature is presented in Chapter 2. Chapter 3 covers the experimental procedure including impact initiation tests and recovery configurations employed. In Chapter 4 the results of experiments are presented along with the discussion of the results; and the relevant conclusions and future work are presented in Chapter 5.



## CHAPTER II

### BACKGROUND

#### *2.1 Reactive/Energetic Material Characteristics*

Energetic or reactive materials traditionally are classified into three categories: Primary explosives, Secondary explosives and Pyrotechnics [7]. These groups vary in sensitivity to ignition, ranging from the extremely sensitive primary explosives like trinitrotoluene (TNT) and cyclotrimethylenetrinitramine (RDX), to less sensitive secondary explosives, and least sensitive pyrotechnics that, instead of exploding, can be tailored to deliver different colors of light and amounts of heat in reaction.

Energetic materials can also be defined in three other categories such as molecular explosives — like TNT,  $\Delta H_R$  (heat of reaction) = -5.4 kJ/g — where the fuel and oxidizer involved in the reaction are present in the same molecule or mixtures such as those containing ammonium perchlorate (AP) and Aluminum. Secondly, metal and air combustion reactions take place when a metal powder is ignited in air. The third group energetic materials involves reactive mixtures in which reactions occur in intermetallic-forming or thermite type powder mixtures including intermetallic-forming nickel and aluminum, titanium and boron mixtures, and aluminum and iron oxide. When these energetic materials are combined in such a way that they maintain structural integrity, they can be employed as structural energetic materials [1, 2]. With their ability to release energy to a system and/or ignite depending on specific conditions, these structural energetic materials allow for different applications other than just explosives or pyrotechnics alone. Furthermore, their initiation and energy release characteristics can be modified based on the volumetric distribution of reactants, density of compacts, material system type, binders, compaction techniques, and other properties.

Tables 1 and 2 list various examples of reactive materials based on thermite and intermetallic systems along with their constituent, theoretical densities and heats of reaction [8].

The corresponding densities and heat of reaction for combustion reactions in various metals are listed in Table 3. The constituent systems listed in Tables 1 - 3 show the ranges of energy released from the various reactions (heat of reaction). Combustion of aluminum and boron metal has amongst the highest heat of reaction (energy per unit mass and volume). It can also be seen that the heat of reaction of several thermite and intermetallic systems is equivalent to that of a primary explosive such as TNT. To better understand reactive materials and their initiation, this chapter will review some thermal, static and dynamic reaction initiation studies discussed in the literature, for the characterization of reactive materials.

**Table 1:** Heats of Reaction of various thermite mixtures [8]

Constituents	$\rho_{TMD}$ (g/cm <sup>3</sup> )	Heat of Reaction (cal/g)	Heat of Reaction (cal/cm <sup>3</sup> )
2Al+B <sub>2</sub> O <sub>3</sub>	2.524	780.7	1971
2Al+Bi <sub>2</sub> O <sub>3</sub>	7.188	506.1	3638
2Al+Cr <sub>2</sub> O <sub>3</sub>	4.190	622	2606
2Al+3CuO	5.109	974.1	4976
2Al+Fe <sub>2</sub> O <sub>3</sub>	4.175	945.4	3947
3Al+Ni <sub>2</sub> O <sub>3</sub>	4.045	1292	5229
Be+CuO	5.119	1221	6249
Mg+CuO	3.934	1102	4336
Ti+2CuO	5.830	730.5	4259
3Ti+2Fe <sub>2</sub> O <sub>3</sub>	5.010	612.0	3066
Ti+Fe <sub>3</sub> O <sub>4</sub>	4.974	563	2800

**Table 2:** Heats of Reaction of various intermetallic forming compounds (\*denotes 1:1 stoichiometric ratio)[8]

Constituents	$\rho_{TMD}$ (g/cm <sup>3</sup> )	Heat of Reaction (cal/g)	Heat of Reaction (cal/cm <sup>3</sup> )
Al+2B	2.607	742	1940
Al+Cu*	5.294	108	573
Al+Ni*	5.165	330	1710
Al+3Ni	6.820	180	1230
Al+Ta*	9.952	56.7	564
3Al+Ta	6.407	35.9	230
Al+Ti*	3.628	240	872
2Al+Ti	3.326	314	1100
2Al+Zr	4.240	267	1130
2B+Ti	3.603	1320	5170

**Table 3:** Heats of Reaction of combustions of various metals [8]

Metal	Oxide	$\rho_{TMD}$ (g/cm <sup>3</sup> )	Heat of Reaction (cal/g)	Heat of Reaction (cal/cm <sup>3</sup> )
Al	Al <sub>2</sub> O <sub>3</sub>	2.7	7422	20040
B	B <sub>2</sub> O <sub>3</sub>	2.5	14050	35120
Ni	NiO	8.90	976.1	8688
Ta	Ta <sub>2</sub> O <sub>5</sub>	16.6	1351	22430
Ti	TiO <sub>2</sub>	4.50	4714	21210
W	WO <sub>2</sub>	19.3	766.6	14790
W	WO <sub>3</sub>	19.3	1096	21150

## 2.2 Thermal Initiation

Thermal initiation of reactive materials has been investigated through the application of either direct heating via laser or hot filament. Differential Scanning Calorimetry (DSC) and

Differential Thermal Analysis (DTA) have also been employed to determine the reaction initiation temperature as well as to perform reaction kinetics studies [9, 10, 11, 12]. The following sections describe the various techniques employed for thermal initiation of reactive materials, provide examples of researched materials, their test set-ups, and the properties tested.

### 2.2.1 Electrical Ignition

Electrical ignition studies of reactive materials have employed an approach similar to that used in resistance welding. Spherical electrodes of opposite charges (positive and negative) contact a reactive foil/material on opposite sides along an axis of radial symmetry as illustrated in the setup shown in Fig. 1, used at the Johns Hopkins University [13]. Current flows from the positive to the negative electrode creating resistive heating through the entire thickness of the material. The resistance heating causes the material to react. After reaction, the amperage and the length of the electrical pulse are used to determine the thermal energy involved in reaction initiation.

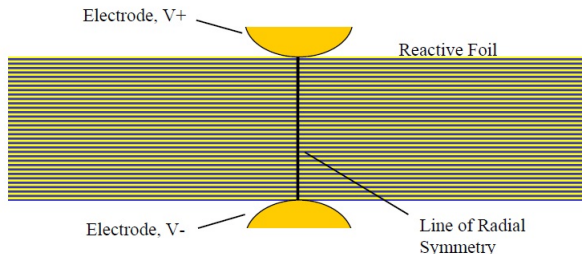


**Figure 1:** Cross-sectional geometry of electrical ignition setup. Electrical current flows from the conductor with the positive voltage (V+) to the one with the negative voltage (V-) across the thickness of either a 20 or 100  $\mu\text{m}$  foil. Figure taken from [13]

Multi-layered Ni+Al reactive foils were examined through electrical ignition and monitored visually in studies performed by Spey [13]. If the samples reacted upon the first electrical pulse, no data was collected. If samples did not react, the current was increased by 10A in each cycle until a reaction did occur. The final amperage necessary to cause a reaction was recorded. Experimental data in comparison with computational data is shown in Fig. 2, where the current necessary to cause reaction is related to the contact radius of the electrode with the foil. Computational/numerical simulations were also performed to

help better understand the ignition process (through the examination of the current and resistive heating) of these reactive foils. The type B foil in Fig. 2 is most similar to the experimental foil samples. It can be seen that the experimental results show an inverse relationship between current and contact area.

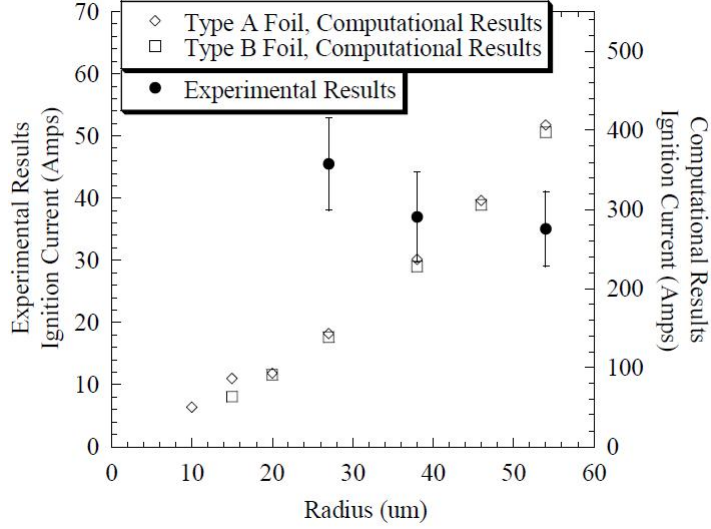


**Figure 2:** Experimental and computational results of ignition current plotted as a function of contact radius experimental results. The error bars represent one standard deviation in the data. The foil tested was similar to the type B foils used in the numerical simulations: 90um Al (Ni-7V) foil with a 50nm bilayer and a 2.25nm intermixed layer thickness. The pulse duration was 50usec. Numerical predictions for type A (2.0nm intermixed layer, 20nm bilayer, 20um thick) and type B (2.25nm intermixed layer, 50nm bilayer, 100um thick) foils are included for comparison. Figure taken from [13]

Such types of ignition current studies have been used to determine the reactivity of a variety of highly-reactive multi-layered fully-dense materials.

### 2.2.2 Filament Ignition

The filament ignition experiment setup employed by Shoshin et al [12], includes a Nickel-chromium filament that is heated in a circuit at the rate of  $10^3 - 10^4 K/s$ . One centimeter of the 4.5 cm long filament is covered with a reactive material paint dispersed in a slurry and dried. While a high-speed pyrometer measures the heat of the uncovered filament as the temperature increases, a photodiode monitors the slurry covered area to denote reaction from ignition by tracing the temperature profile and the spike in temperature at reaction

with respect to time [12], [10], [14]. A schematic of the setup employed by the Dreizin group to study the reactivity of nanothermite mixture is shown in Fig. 3.

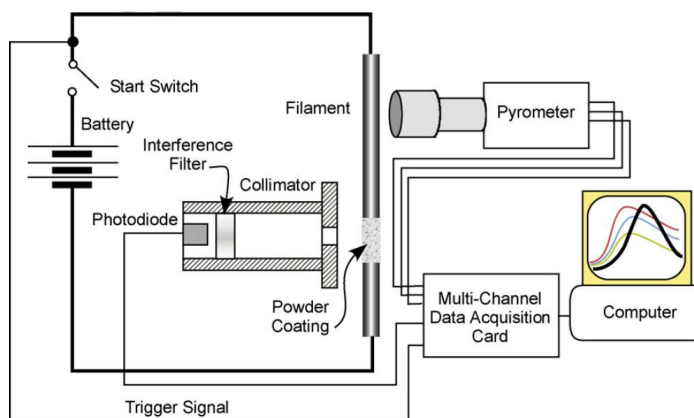


**Figure 3:** Filament Ignition Experimental Setup [14]

The reaction is observed visually with the sight of flame/smoke from reaction in addition to the photodiode in place tracing the temperature rise associated with the reaction. An example of the photodiode trace can be seen in Fig. 4, illustrating the capture of the initiation events in the reaction and formation of  $\text{Al}_{0.80}\text{Ti}_{20}$  alloy.

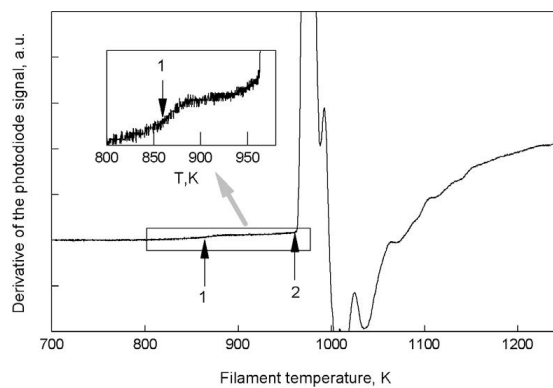


**Figure 4:** A photodiode trace showing spike in temperature associated with the gray arrow displaying a blown up portion of the events in arrow (1) and (2) leading to reaction and formation of  $\text{Al}_{0.80}\text{Ti}_{20}$  alloy [12]

### 2.2.3 Differential Scanning Calorimetry and Differential Thermal Analysis

Differential scanning calorimetry (DSC) and differential thermal analysis (DTA), measure the change in heat content or thermal properties [15] as samples are heated at a controlled rate until a reaction occurs. The reaction initiation indication is denoted by a peak corresponding to an endo- or exothermic heat release during the temperature time scan [16]. The release of energy, which is in the form of “spikes” associated with exothermic reactions, is recorded with the DSC or DTA and corresponds to the onset temperature of reaction initiation.

An example of the reaction observed during heating in a DSC can be seen in Fig. 5, where different stoichiometries of lithium nickelate plus electrolytes indicate reaction initiation at different onset temperatures. In studies performed by Umbrajkar et al [9], Al-rich mixtures Al-MoO<sub>3</sub> thermite nanopowders were examined using a Netzsch Simultaneous Thermal Analyzer STA409 PC, with baseline correction performed using fully reacted samples. Traces of samples heated from room temperature up to 1200K with heating rates ranging from 1 to 40K/min are shown in Fig. 6. It can be seen that the exothermic peaks corresponding to various reactions are shifted to higher temperature (including the main exothermic reaction) with increasing heating rates. The main exothermic reaction obtained above 800K corresponds to the onset of reaction following the melting of aluminum.

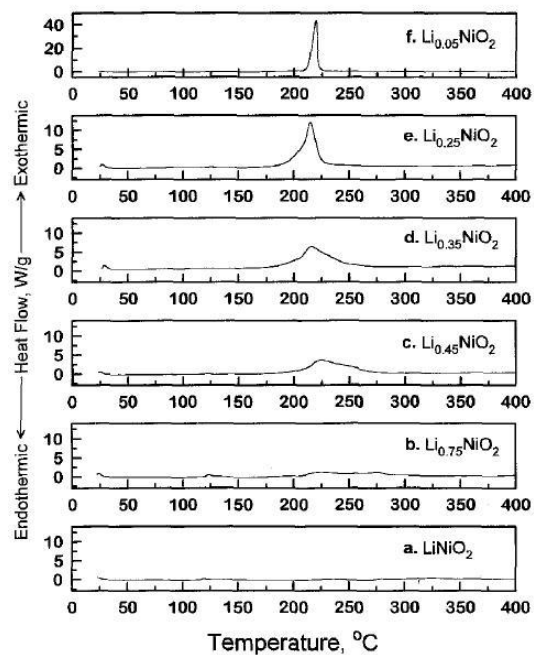


**Figure 5:** DSC traces obtained for  $\text{Li}_x\text{NiO}_2$  plus electrolyte showing variation in reaction initiation temperature with increasing stoichiometries of Li [16]

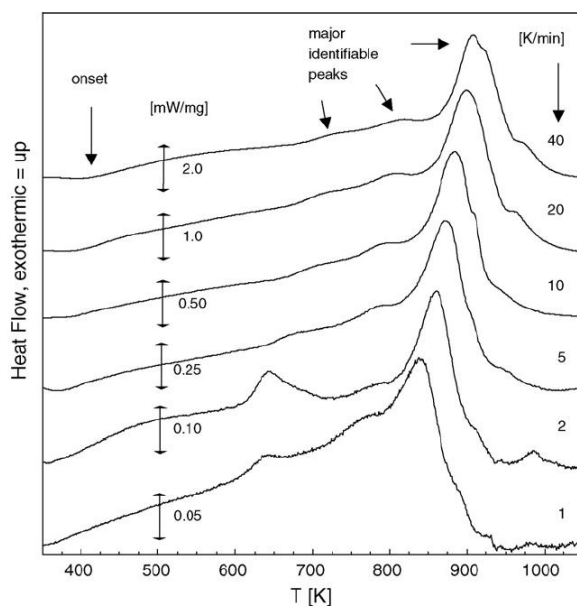


**Figure 6:** Baseline-corrected DSC traces collected for nanocomposite powder with bulk composition  $\text{Al-MoO}_3$  at heating rates ranging from 1 to 40 K/min. The traces were scaled to fit on the same plot; the vertical scale applicable to each trace is shown in units of mW/mg [9]



### 2.2.4 Laser Ignition

Slightly different than the previous thermal initiation techniques, electrodynamic levitation of reactive particles involving the use of a laser set up can also be employed to study ignition of reactive materials [11, 17]. In the setup described by Legrand et al. [17], charged particles are placed in an electrodynamic levitator (Fig. 7) located in a high-pressure chamber.

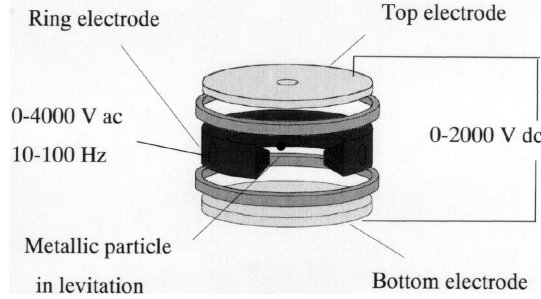


**Figure 7:** Electrodynamic levitator from Shafirovich et al [11]

The levitator is comprised of top and bottom electrodes and a one ring electrode where the particle is “levitated” or suspended. Then, a CO<sub>2</sub> laser is used to heat the particles until ignition, at which point the laser is turned off. In addition to monitoring the laser on/off records, ignition delay and burning times are calculated using a photomultiplier. The entire setup can be seen in Fig. 8, where magnesium (Mg) and Mg-Al particles studied by Legrand [17] were tested to determine the critical chamber pressure needed to cause ignition/combustion.

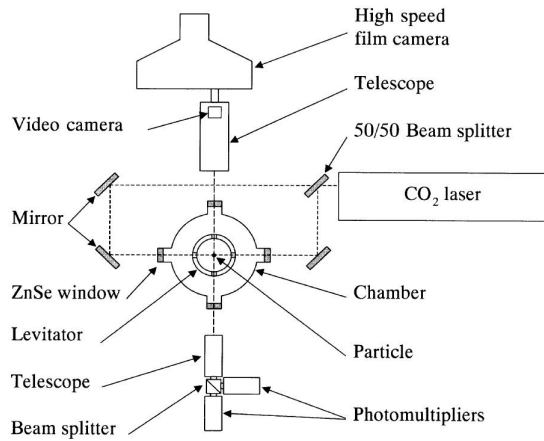


**Figure 8:** Experimental setup for laser ignition of levitated particles from Sharfirovich et al [11]

The data observed by the photomultipliers for the reaction light emission intensity is shown in Fig.9, while Fig. 10 displays the ignition probabilities as a function of the CO<sub>2</sub>-Ar environment and chamber pressure for Mg particles. These figures show that light emission can occur during a reaction (Fig.9) and there is some relationship between the experimental chamber environment on the reaction initiation (Fig. 10).

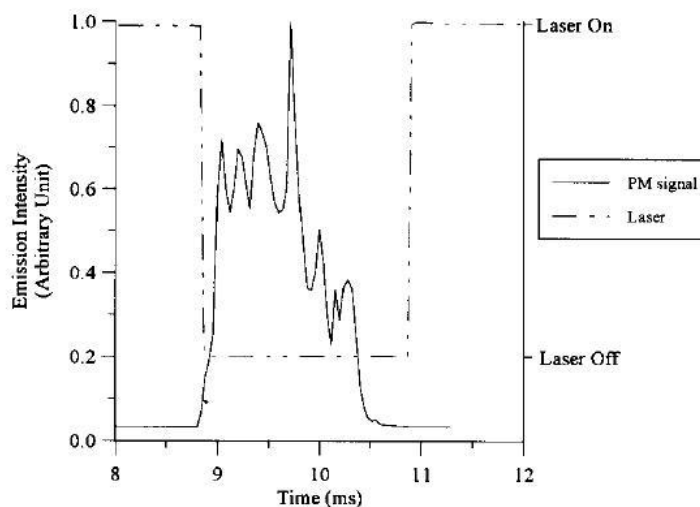


**Figure 9:** Typical record of the light emission during the burning phase of spherical Mg particles (50-63  $\mu$  m) in CO<sub>2</sub> at 1 MPa. Figure taken from [17]

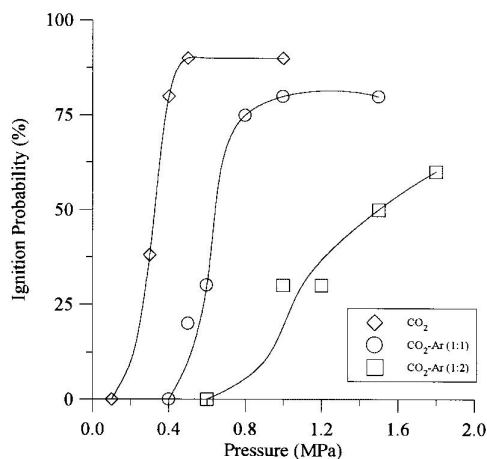


**Figure 10:** Ignition probability of spherical Mg particles (5063  $\mu$ m) in different CO<sub>2</sub>Ar mixtures as a function of total chamber pressure. Figure taken from [17]

## 2.3 Impact Initiation

Impact initiation has been used thoroughly to characterize what aspect of reactive materials and their loading conditions are critical in the initiation processes. The following subsections describe various experimental setups used for reactive materials studies to characterize their dynamic energy release, dynamic yielding, effects of sample orientation and shear, particle size and density, and shock-loading, as well as the reaction product characterization.

### 2.3.1 Drop Weight Test Setup

The drop weight test setup involves a weight suspended, normally above a platform at a specified height, and released to impact another plate holding the reactive material sample. In these tests, the samples can be impacted in powder or pressed form arranged in various orientations to gain information on the dynamic impact response and reactants. Walley et al. [7] have determined the dynamic impact response of five different thermite samples. Thermite samples (Fig. 11) were pressed into right-circular disks, pre-sheared disks to 30 degree incline, and left “as-is” in powder form. The reactivity of the thermite samples are compared under normal axial impact (Fig. 12) and by shearing effect on reaction initiation, where pre-sheared disks (Fig. 13) are impacted in the normal axial setup and right-circular disks impacted at a 30 degree incline (Fig. 14) [7]. A high speed camera is used to record the impact with a light path through transparent anvils and mirrors.

name	composition
SR 40	20% aluminium (heavy, grade 1, special type B) 20% silicon (4 $\mu\text{m}$ or less) 60% potassium nitrate (125 $\mu\text{m}$ )
SR 41	20% boron powder (amorphous, <i>ca.</i> 90%) 10% silicon ( <i>ca.</i> 8–12 $\mu\text{m}$ ) 70% potassium nitrate (all pass 63 $\mu\text{m}$ BSS)
SR 812	50% aluminium (heavy, grade 1, special type B) 50% potassium perchlorate (125 $\mu\text{m}$ )
SR 813	40% aluminium (heavy, grade 1, special type B) 60% potassium perchlorate (125 $\mu\text{m}$ )
Cu(III)O+Al	

**Figure 11:** Thermite Compositions in Drop Weight Experimentation taken from [7]

With the use of the Drop Weight Tests, it was found that reaction was more easily attained in the pressed compacts, than the loose powders without additives, and the pressed

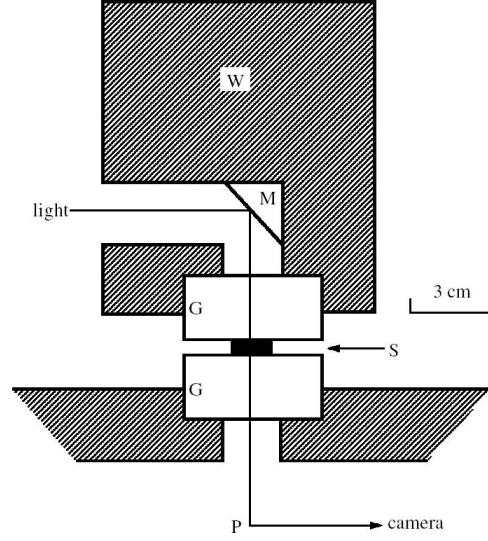


**Figure 12:** Schematic of the high-speed photography drop-weight apparatus used for normal-impact tests.  $W$  is the weight,  $M$  is the mirror,  $G$  is the glass anvils,  $S$  is the specimen, and  $P$  is the prism [7]

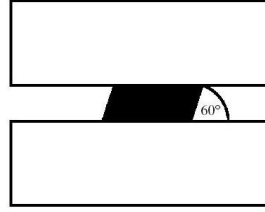


**Figure 13:** Schematic of pre-sheared drop-weight experiment setup [7]

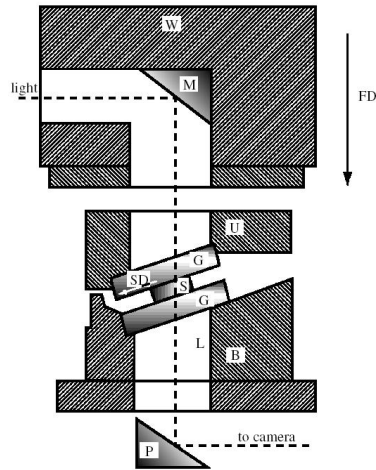
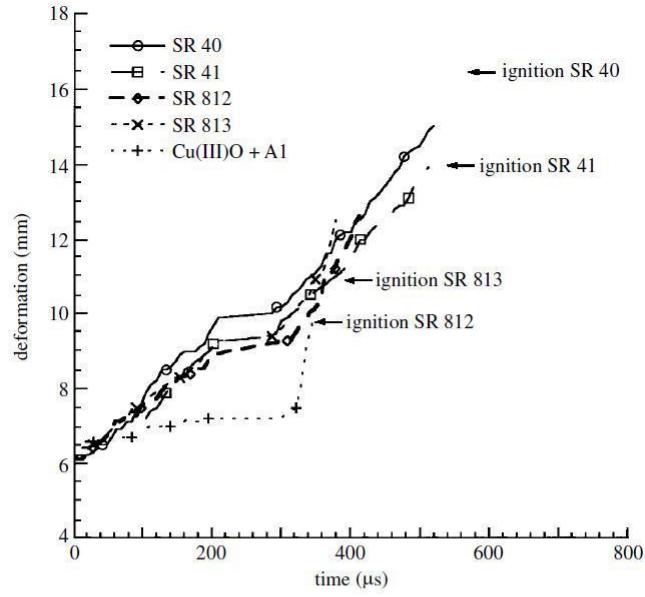
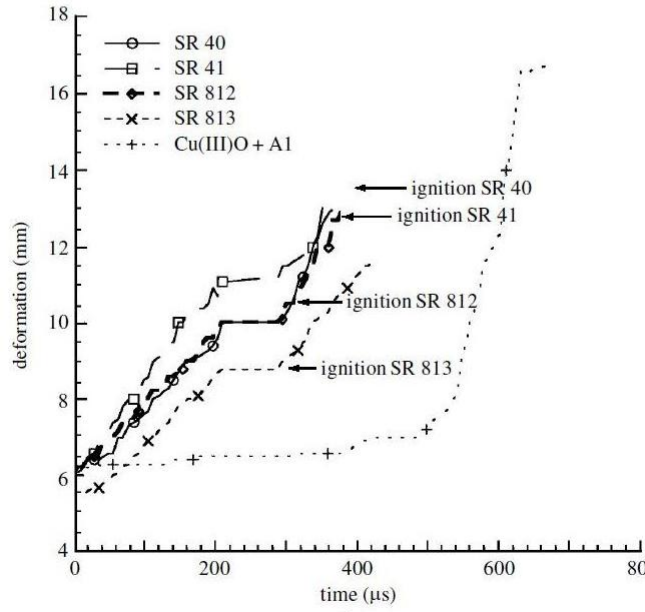


**Figure 14:** Schematic of inclined drop-weight apparatus.  $L$  is the light path,  $B$  is the base,  $FD$  is the fall direction of the weight,  $U$  is the upper (sliding) section of the anvil, and  $SD$  is the slide direction of the upper glass anvil [7]

powders were more reactive than those with polycarbonate powder mixed in. Likewise, the “pre-sheared” compacts were more reactive than those subjected to normal or “normal-inclined shear” impact tests. The deformation verses time curve showing points of ignition for the five different thermite mixtures can be seen in Fig. 15 (a) and (b). In the case of the right circular (a) and pre-sheared(b) pressed samples respectively (the inclined samples were less sensitive, than both the right circular and pre-sheared experimental setups and was omitted). These graphs show that the plastic deformation of samples happens faster in the pre-sheared tests than with the right circular; leading to a correspondingly faster ignition for most of the thermite systems tested. The results indicate that shearing and sample orientation play a role in the reactivity in reactive materials.



(a)



(b)

**Figure 15:** Deformation versus time curves for right-circular (a) and pre-sheared (b) disks. The times at which ignition is first visible on the high-speed photographic sequences is marked on the graph for the various compositions [7]

### 2.3.2 Mechanical Lever Impact Initiation

Figure 16, is the schematic of the lever-drop-weight impact test setup used to study initiation of reactive foils of Ni+Al [13]. Operated from an axle, a lever with an impactor tip (outfitted from hardness tester tips) is lifted to a certain height and dropped in a circular path towards the targeted sample. An oscilloscope connected to a potentiometer on the axle records the position of the arm based on the voltage, and from here the kinetic and potential energies are measured from the drop and rebound after the drop, respectively. This act was continued from increased heights until reaction occurs and the net energy (kinetic energy - potential energy) is recorded. The net energy for reaction initiation can be seen in Fig. 17 to increase, as the Ni+Al foil bi-layer spanning and total thickness increase.

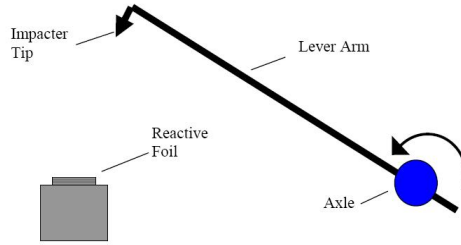


**Figure 16:** Geometry of mechanical lever impact ignition. The lever arm setup rotates about the axle as the impactor tip falls onto the reactive foil sample. A potentiometer attached to the axle records its position. Figure taken from [13]

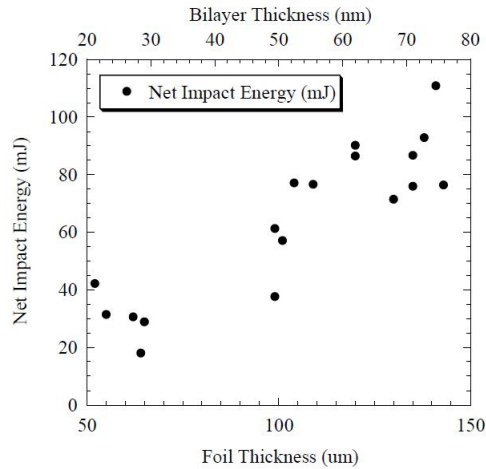


**Figure 17:** Results of mechanical lever-arm impact tests. For a foil of Al Inconel with 112nm with excess Inconel on each side. The reactive foil rested on the bulk metallic glass surface and the impact tip was a 1/16 radius WC sphere. Figure taken from [13]

### 2.3.3 Taylor Rod-on-anvil Impact Test

The rod-on-anvil impact test was developed by Sir Geoffrey Taylor in 1947; where cylindrical (flat ended) projectiles of varying materials were fired from guns perpendicularly into a high strength, rigid, flat and polished steel anvil, in order to determine the dynamic yield stress. The dynamic yield stress was determined by measuring the velocity and the deformed and undeformed portions of the projectile. [18]. Torres et al. [19], used the Taylor Test to characterize some dynamic material properties of Eglin steel rods. Steel samples were formed into cylindrical rods and fired at a hardened flat steel anvil at velocities ranging from 155 m/s to 210 m/s (examples of impact-face deformation of the sample can be seen in Fig. 18).

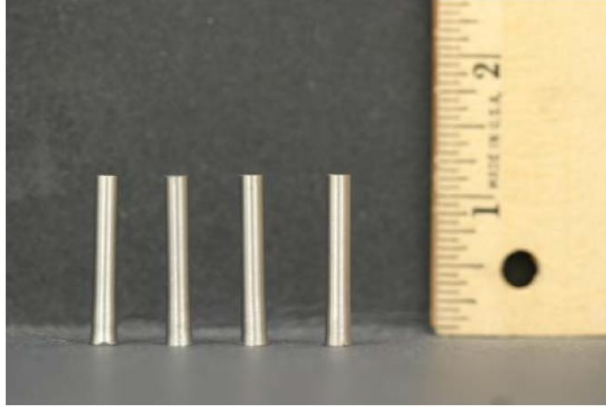


**Figure 18:** A series of post-test 164-caliber specimens. The velocities ranged from 210 m/s to 181 m/s, from left to right. Figure taken from [19]

Based on the change in geometry of the deformed sample, corresponding impact velocity and material densities, average values of the dynamic yield stress and strain rate can be calculated. An example of the calculated dynamic yield stress versus the strain-rate for samples of 164 and 215 caliber are shown in Fig. 19 indicating the typical trend of increasing strength until leveling off when the strain rate reached  $10^4 s^{-1}$  to  $10^5 s^{-1}$ .

Ames [20] used the rod-on-anvil impact tests to characterize the reaction initiation properties of reactive materials. The energy release characteristics of energetic materials were examined under impact initiation, where a self-sustained reaction can be observed from the mechanical work of impact through the use of the Taylor rod-on-anvil test. In these



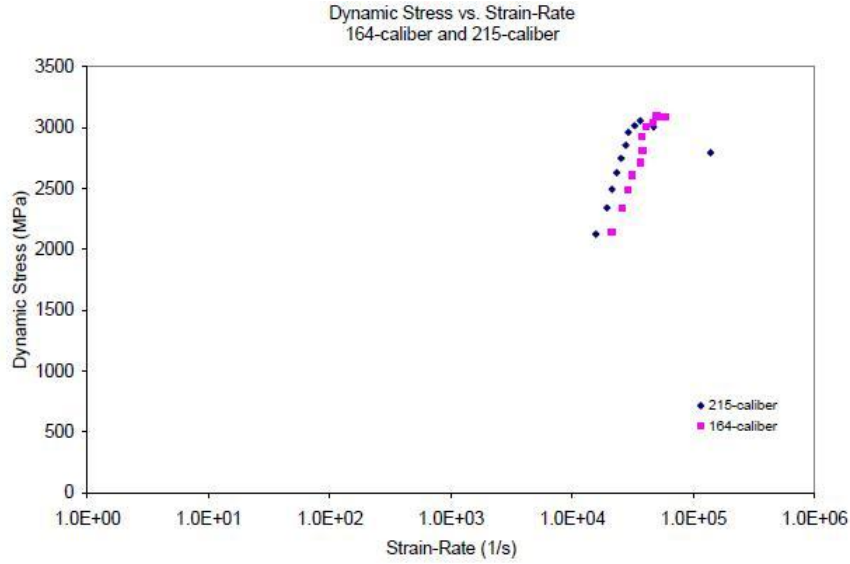


**Figure 19:** Dynamic stress estimates for the 164-caliber and 215-caliber specimens. Figure taken from [19]

experiments, various metal powders mixed with a polymer binder were pressed close to TMD (Theoretical Maximum Density) and accelerated to impact the rigid anvil. Reaction initiation was indicated in the form of smoke release that was captured with high speed imaging.

Examples of images of impacted samples of Polytetrafluoroethylene-Aluminum (PTFE-Al) mixtures are shown in Figures 20 and 21 displaying both fracture and shear initiated reactions. As shown in Fig. 20 a gradual increase of impact speed, from 158 m/s to 160 m/s results in fracture, and increasing the velocity to 163 m/s results in fracture followed by smoke generation indicating ignition of the energetic material. The fracture process and exposure of clean fracture surfaces have been speculated to contribute to reaction. However, fracture may not be the lone contributor needed to sustain a reaction. The high shear areas shown in Fig. 21, where the shearing resulting from deformation occurring at high strain rates ( $10^4 s^{-1}$  and higher) at impact, creates temperatures and pressures conducive to reaction initiation.

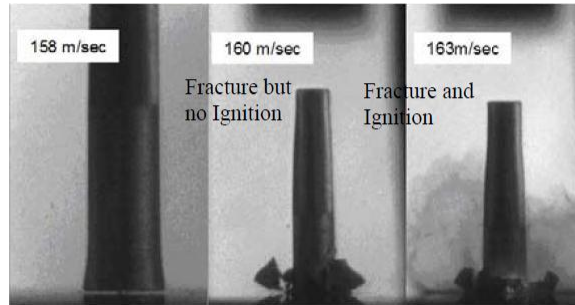


**Figure 20:** Images of PTFE-Al samples shot in Taylor test experiments at three different velocities showing progression of deformation at 158 m/s, fracture at 160 m/s, and fracture followed by reaction at 163 m/s (from [20])

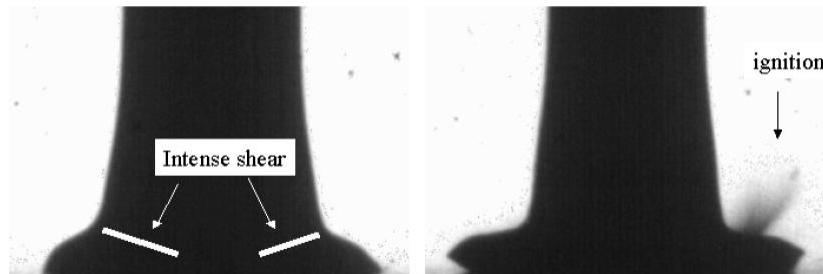


**Figure 21:** Shear-induced ignition evident in PTFE-Al Taylor rod test (from [20])

#### 2.3.4 Dynamic Energy Release Characterization using Pig Test

In an effort to characterize the impact-initiation phenomena and the release of energy from reactive materials, Ames and coworkers [20], have employed the so called "Pig test". The Pig test employs a high speed camera to monitor the reaction light emission and pressure transducers to determine the impulse from the reaction. The experimental setup resembles a Taylor impact test where a reactive material projectile is accelerated perpendicularly to impact a rigid anvil in an experimental chamber. This chamber's opening is covered with a thin sheet of a mild steel (referred to as a target skin, usually  $\frac{1}{16}$ " thick) and is penetrated by the projectile before impacting the anvil, as shown in Fig.22.

The reactive material projectile, perforates through the target skin and fragments. These fragments impact the rigid anvil (and can sometimes react when perforating through the target skin or in flight). The fragments impacting the rigid anvil react, cause a spike in the chamber pressure. Actual images obtained from such an experiment can be seen in Fig. 23 revealing light emission due to reaction and pressure pulse recorded by the transducers over a period of up to 12 ms. Depending on the reactive material systems, reaction have been observed to occur upon initial penetration of the skin, upon impact of the fragments with the anvil, and also as the combustion wave propagates backwards and causes unreacted finer fragments to burn resulting in an after-burn type effect.

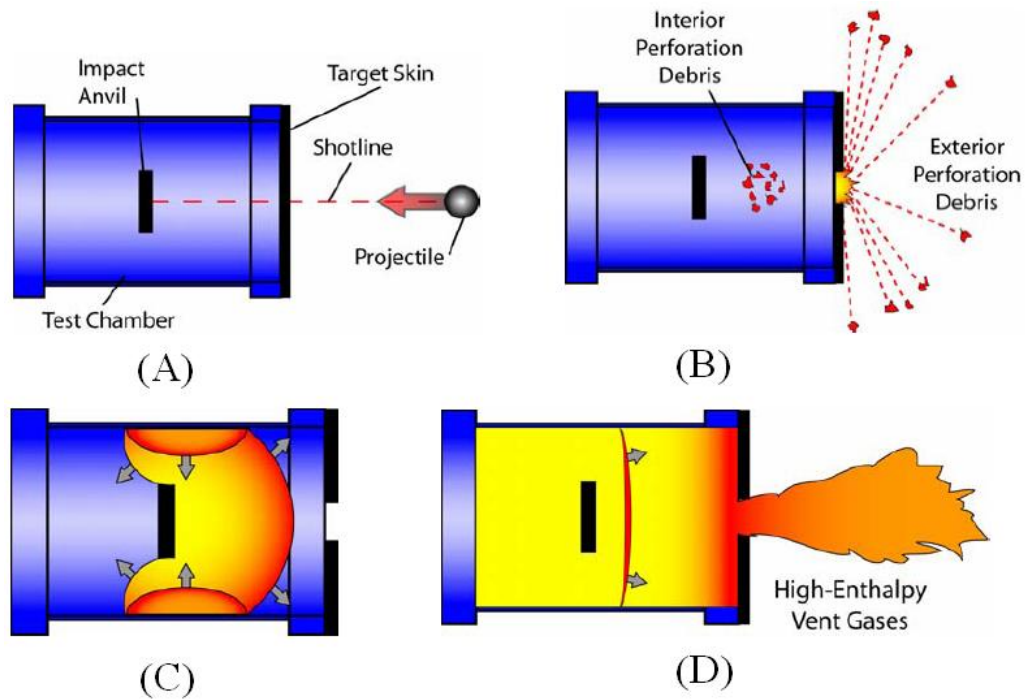


**Figure 22:** Schematic of the Pig test used for dynamic energy release characterization: (A) Test chamber set up with projectile being accelerated towards the target. (B) Projectile impacts target skin, fragments and continues towards rigid anvil impact. (C) Fragments impact and react creating detonation-like blast wave. (D) Unreacted materials cause the after burn of particles interacting with trapped air in fragments and ambient air. Figure from [20]

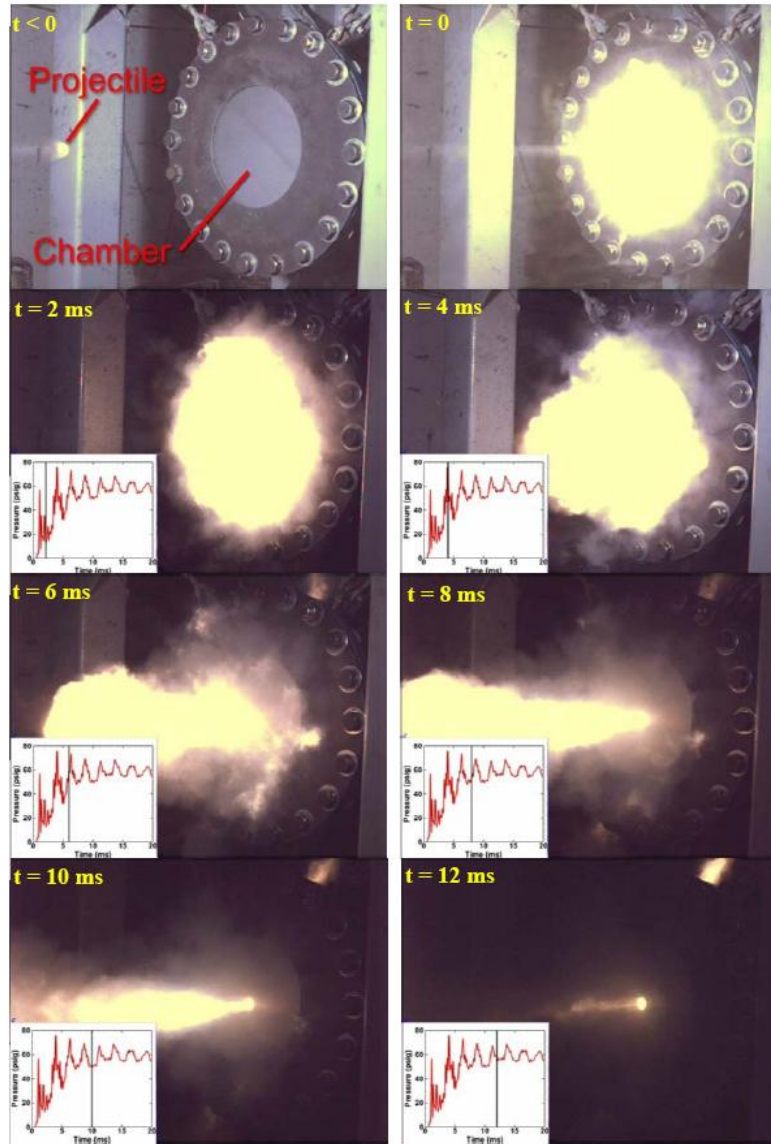


**Figure 23:** Highspeed camera images of Pig test with the corresponding pressure graphs in lower left corners of the image. Figure from [20]

In characterizing the material systems the efficiency and relative energy release were tested. The efficiency is the ratio between the calculated mechanical (kinetic) and theoretical (chemical) energy. Figure 24 displays the efficiency of each material system studied in a range of velocities from 1.2 - 2.4 km/s. Here, the data shows two things — first, the reactivity for most of the materials systems is dependent upon the energy of the fracture process (correlating with the increase of speed of impact). Secondly, the energy efficiency at an observed critical threshold (between 1.8 and 2.4 km/s shows no significant increase.

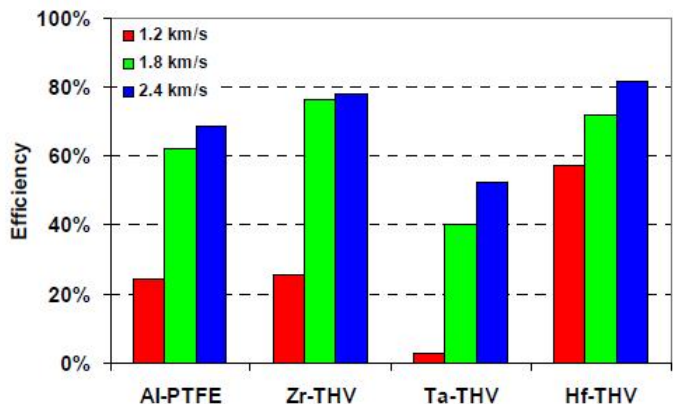


**Figure 24:** Reaction efficiencies of various metal-polymer energetic materials tested at different velocities showing ratio of efficiency of the calculated kinetic energy during the fracture process at impact vs chemical/theoretical energy at impact. Figure from [20]

The relative energy release in Fig. 25, is a comparison of the energy released during reaction of over 20 materials (intermetallics, metal powders, fluoropolymer binders, epoxy binders, thermites, and others) plotted versus their density. These materials were normalized by PTFE-Al's density and accelerated to the same impact velocity of 6,000 ft/s. Figure 25 shows that density is a stronger component in measured energy release than theoretical energy of the different material system contents.

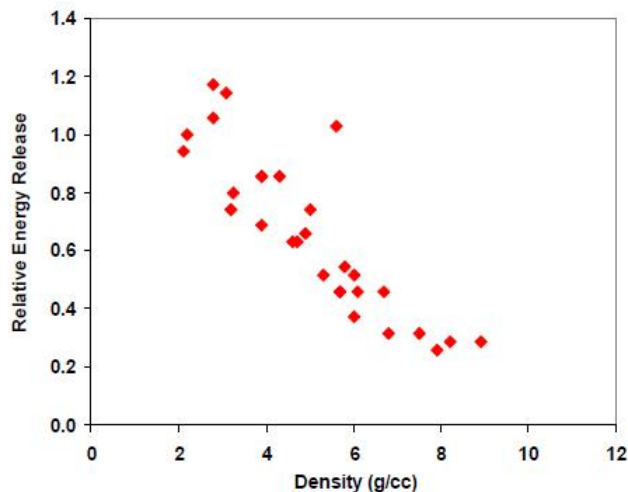


**Figure 25:** Relative energy release for 6,000 ft/s of various energetic material systems showing the density effect of material systems. Figure from [20]

### 2.3.5 Shock Compression of Reactive Powder Mixtures

Through the application of dynamic pressure or shock compression, materials can be studied in thermodynamic regimes not readily made possible through other means. The shock compression of materials is dominated primarily through the shear stress/strain effects aided both by the generation of crystalline defects and accelerated kinetics of physical and chemical changes creating radically modified structures. Novel compounds and alloys, and metastable phases can be formed through such chemical and physical changes occurring during shock compression of materials [21, 22, 23, 24].

Shock induced decomposition of compounds, chemical reactions involving two or more highly exothermic components, and oxidation; reduction thermite reactions have been thoroughly investigated for synthesis of novel materials as well as high density energetic materials [25, 26, 27, 28, 29]. The interest in these types of reactions have been driven by multiple goals, but mainly from the desire to understand the mechanisms of reaction initiation for synthesis of novel phases, and to provide the ability to manipulate energy release characteristics in the case of next generation of energetic materials [22, 30, 31, 32].

### 2.3.5.1 Shock-Induced Reactions

Shock compression is used to characterize the shock properties of reactive materials and induce or assist in reaction initiation. Eakins and Thadhani [33], used parallel plate impact experimentation to shock-induce reaction in nickel flake and spherical aluminum powders (1:1 mix by volume) with loading up to 6 GPa. Packed at a 42 percent  $\pm 2$  TMD, the Ni+Al powder is loaded in between two PVDF (polyvinylidene difluoride) stress gauges used to attain time-resolved measurements of the Hugoniot (equation of state of a material/material system relating shock velocity and pressure) data. The experimental setup can be seen in Fig. 26 where a Cu or W driver plate, on the impact face of a flier impacts the Cu containment ring holding the powder and the PVDF gages, that measures pressure and time data during the shock phenomena.

The experimental data points from the tests were plotted by stress vs velocity with overlays of the calculated Hugoniots for inert Ni+Al, NiAl, Ni<sub>3</sub>Al, and NiAl<sub>3</sub>. The reaction products can be assumed based on the calculated curves in comparison to the plotted data shown in Fig. 27. The points below 3.5 GPa fit the curve rather well, and the point above (in the area of 5.4 GPa) fit well with in the realm of reaction products, although the actual characterization and product distribution could not be determined in this work.

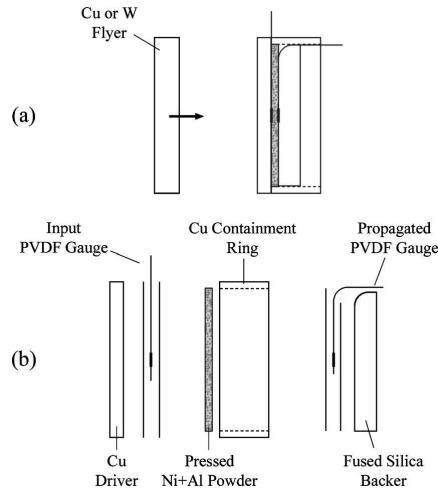


**Figure 26:** Illustration of the parallel-plate impact experiment, showing (a) flier-target assembly and (b) exploded view of the sample assembly. The input and propagated PVDF stress gages are in direct contact with the powder layer of nominal thickness. From [33]



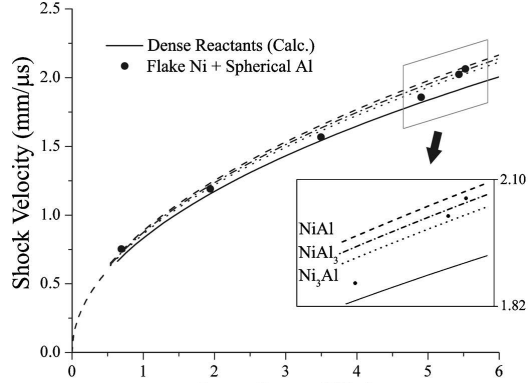


**Figure 27:** Plot of shock velocity and input stress for the flake mixtures up to 6 GPa. The experimental data (closed circles) follow the calculated inert response (solid line) up to 3.5 GPa. The data at higher stresses (inset) indicate a deviation toward the calculated reaction product curves (dashed lines) suggesting the occurrence of shock-induced reaction. From [33]

#### 2.3.5.2 Reaction Product Characterization

Reactive materials are often heterogeneous mixtures of components in various stoichiometries, particle sizes, and shapes. These variables influence how the reactions are initiated, the reaction products formed, and the amount of energy necessary to cause a reaction. Recovery experiments have been performed to characterize the materials involved and to identify the reaction products created during the reaction event.

Characterization can be done through X-ray diffraction (XRD), scanning electron microscopy, and transmission electron microscopy to determine not only the reaction products formed but also the state of unreacted constituents. X-ray diffraction analysis in particular has been used for the characterization of the extent of reaction and reaction products that are formed. An example of an XRD for  $5\text{Ti}+3\text{Si}$  can be seen in Fig. 28 where after shock compression the product phase results in the formation of  $\text{Ti}_5\text{Si}_3$ , and no unreacted constituents.

Shock recovery experiments can be performed to retrieve material in order to characterize the as-shocked materials using specifically designed fixtures including the Sandia Bear fixtures, the 12-capsule Sawaoka shock recovery fixture, and the Georgia Tech 3-capsule fixture [35] [36]. The Sawaoka 12-capsule shock recovery fixture can be seen schematically in Fig.29.

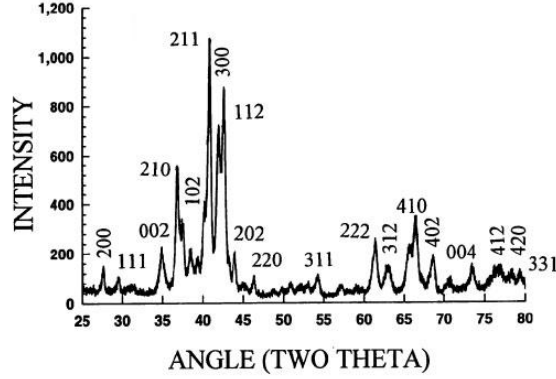


**Figure 28:** XRD spectrum shows the product to be  $\text{Ti}_5\text{Si}_3$ . From Thadhani et al [34]

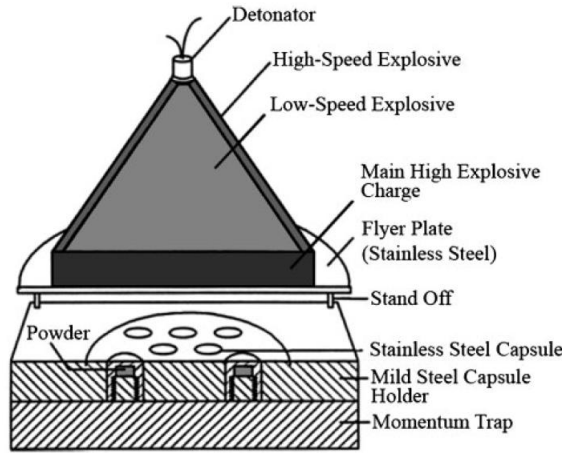


**Figure 29:** Schematic detailing the 12-capsule Sawaoka fixture in used in shock recovery experiments. Powder samples are loaded into each of the 12 steel capsules, and held within a steel capsule holder plate. The uniform detonation of a main charge launches a thin metal flier plate, which subsequently impacts the holder plate, driving a shock through capsules and compressing the powders. The rugged design permits recovery of the powder compacts for post-shock characterization. From Song and Thadhani [37]

## 2.4 Background Conclusions

Structurally energetic materials are unique in their ability to tailor to their level of sensitivity to stimuli, in various forms, and still retain structural properties. A breadth of work has been done on reactive materials including initiation and characterization techniques on a multitude of reactive material systems. Specifically pertaining to reaction materials with large differences in constituent density and strength, for example, with  $\text{W}+\text{Al}$ ,  $\text{Ta}+\text{Al}$ , and

Ni+Al equi-volumetric systems, the effects of material characteristics can be explored. It is intended to use, and modify in some cases, the techniques found in this background chapter including initiation, measurement, and characterization of reactive materials to determine the threshold of reaction initiation, using a modified Taylor rod-on-anvil impact test, and implement novel recovery apparatus to retain reaction products for the characterization of various equi-volume Al-based intermetallic-forming materials.

## CHAPTER III

### EXPERIMENTAL PROCEDURE

#### *3.1 Objectives and Approach*

The objectives of this work are to determine the threshold energy for reaction initiation for each of the intermetallic-forming systems, determine reaction products, and to determine if the reactions are dominated by anaerobic or oxidation process. This will be done through the investigation of impact initiated reactions in Al-based reactive mixtures including W+Al, Ta+Al, Ni+Al, and pure Al. Impact experiments were performed on samples using a modified version of the Taylor impact test setup. The samples were prepared by mixing powders in desired stoichiometric ratios and statically pressing into right-cylindrical pellets before mounting those onto right-cylindrical copper projectiles to be fired with a gas gun. The transient deformation of the samples at impact was observed and reaction was captured with high-speed imaging as a function of different projectile kinetic energies and chamber atmosphere (air or vacuum).

#### *3.2 Reactive Materials Systems*

The Al-based intermetallic forming reactive material systems (Ni+Al, Ta+Al, W+Al, and Al) selected in this work, have characteristic properties that are of interest with regards to the understanding of impact initiated reactivity, and their use as structural energetic materials. In Table 4 some of the relevant properties of the constituents for each of the individual systems are included in addition to their heats of formation for intermetallic reactions, as well as that for the combustion reaction. With respect to intermetallic systems, Ni+Al has the highest heat of reaction, while the W+Al and Ta+Al systems have the highest density (mass). The Table also lists the constituent properties, which illustrate that the W+Al has the highest mismatch (difference) in strength and density. The strength difference between constituents influences the degree of mixing due to plastic flow of constituents. On the other hand the density difference between constituents influences the ratio of the constituents in

terms of the weight or volume. For example, as shown in Tables 5 and 6, the Ni+Al stoichiometry ratio of 3 : 1, corresponds to 6.53 parts of Ni for every 1 part Al by weight, and 1.98 parts of Ni for every 1 part Al by volume. Likewise, the equistoichiometric Ni+Al ratio corresponds to 2.18 parts of Ni for every 1 part Al by weight, and 0.66 parts of Ni for every 1 part Al by volume. In other words, the equistoichiometric Ni+Al mixture which represents the system with the highest heat of reaction amongst all Ni+AL systems, is more enriched with Al than with Ni on a volume basis, which can limit the degree of localized and bulk deformation occurring in the system.

**Table 4:** Table listing relevant properties of Al, Ni, Ta, and W [38],[39],[40]  $\delta$ , [8]  $\alpha$ . The associated symbols by references refer to the contributed data in this table. \* Denotes values from work of S. Du

	Aluminum (Al)		Nickel (Ni)		Tantalum (Ta)		Tungsten (W)	
Density (g/cm <sup>3</sup> )	2.69		8.9		16.6		19.4	
Atomic Weight (g/mol)	26.98		58.7		180.94		183.85	
Crystal Structure	FCC		FCC		BCC		BCC	
Melt Temperature (°C)	660.4		1453		2996 $\delta$		3695 $\delta$	
Elastic Modulus (GPa)	62		207		186		411	
Yield Strength (MPa)	89		59		170		560	
Heat of Reaction (cal/g) $\alpha$	Al <sub>2</sub> O <sub>3</sub>	7422	NiO	976.1	Ta <sub>2</sub> O <sub>5</sub>	1351	WO <sub>2</sub>	766.6
			1Al+1Ni	330	1Al+1Ta	56.7	3Al+1W*	31.8

The individual Ni, Ta, W, and Al powders investigated in this work were all spherical of -325 mesh ( $\approx$  44 microns) particle size and of 99.8 percent purity. Figure 30 (a-d) shows SEM images revealing the morphology and distribution of the various powder mixtures.

**Table 5:** Intermetallic-forming Reactive Material system mass ratios for selected stoichiometries. EV stands for equal-volumetric values and ratios are represented with  $M : Al$  where  $M$  represents other constituent in Al-based material system.

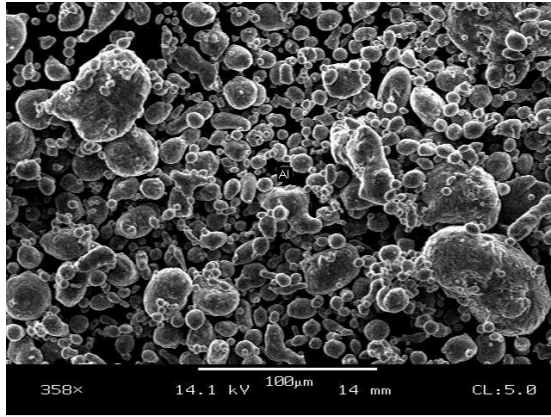
Stoichiometric Ratio	Ni+Al	W+Al	Ta+Al
3 : 1	6.53 : 1	20.4 : 1	20.1 : 1
1 : 1	2.18 : 1	6.81 : 1	6.71 : 1
1 : 3	.73 : 1	2.27 : 1	2.24 : 1
3 : 2	3.26 : 1	10.2 : 1	10.1 : 1
EV	3.31 : 1	7.19 : 1	6.19 : 1

**Table 6:** Intermetallic-forming Reactive Material system volume fractions for selected stoichiometries showing the non-aluminum constituent volume fraction values. EV stands for equal-volumetric values and ratios are represented with  $M : Al$  where  $M$  represents other constituent in Al-based material system.

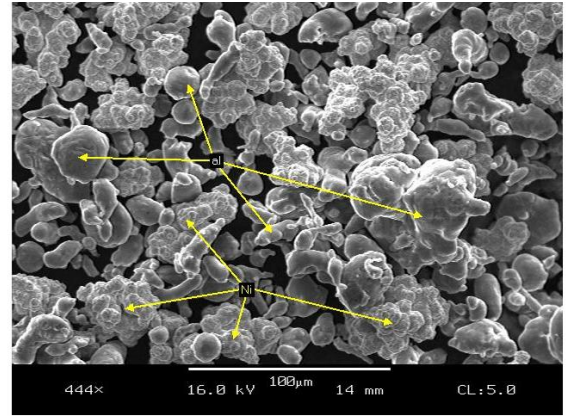
Stoichiometric Ratio	Ni+Al	W+Al	Ta+Al
3 : 1	1.98 : 1	2.85 : 1	3.26 : 1
1 : 1	.66 : 1	.95 : 1	1.08 : 1
1 : 3	.22 : 1	.32 : 1	.36 : 1
3 : 2	.99 : 1	1.43 : 1	1.63 : 1
EV	1 : 1	1 : 1	1 : 1

**Table 7:** Intermetallic-forming Reactive Material system densities at selected stoichiometries in  $g/cm^3$ . EV stands for equal-volumetric values

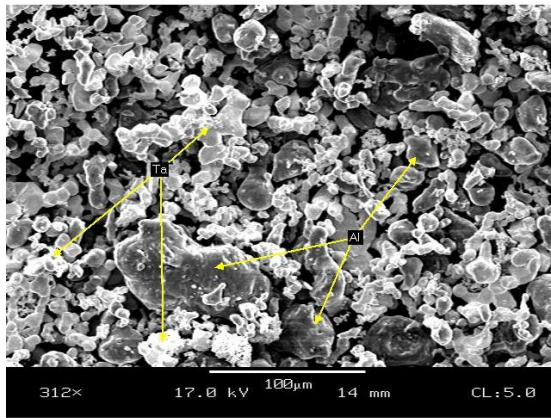
Stoichiometric Ratio	Ni+Al	W+Al	Ta+Al
3 : 1	6.82	15.03	13.38
1 : 1	5.16	10.81	9.97
1 : 3	3.82	6.71	6.41
3 : 2	5.78	12.49	11.35
EV	5.80	11.03	9.68



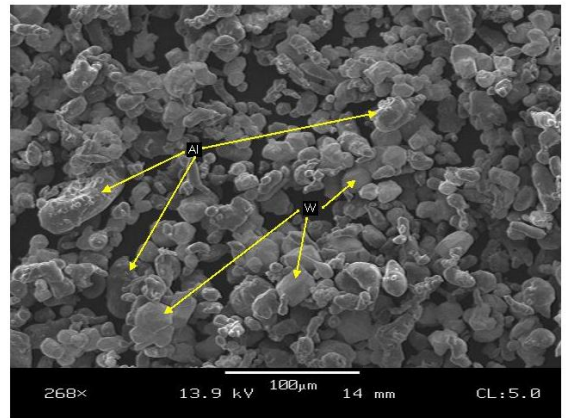
(a)



(b)



(c)



(d)

**Figure 30:** SEM images showing the spherical morphologies of (a) Al and each of the constitutive mixtures (b) Ni+Al (c) Ta+Al and (d) W+Al

### ***3.3 Sample Mixing and Compaction***

The pure metal powders (Ni, Ta, W, and Al) were weighed according to the molar ratio required for an equi-volumetric mixture. It should be noted that the maximum heat of reaction for the various Al-based intermetallic mixtures investigated often correspond to equi-atomic stoichiometry, which then skews the volumetric distribution in Al-rich mixtures varying contents due to differences in densities. Hence, in this work, equi-volumetric mixtures were investigated to maintain similar volume content of Al. The powders were baked at 100°C in a vacuum oven to remove moisture for 24 hours prior to mixing. The individual powders were combined in equi-volumetric ratios by pouring the pre-massed equal volume amounts of respective Ni and Al, Ta and Al, and W and Al mixtures into a container, which was placed directly in an Argon-filled glove box and allowed to settle overnight. On occasion the powders were stirred to release any trapped atmospheric gases as well. Before removing powders from the glove box, an air-tight seal (tape) was applied to each container. The powders were then mixed using a V-blender for at least 24 hours.

Quasi-static pressing of powder mixtures was performed after they had been fully mixed. The powders were compacted using a punch-die assembly that pressed cylinder-shaped pellets with a diameter of 3.175 mm (.125") and a sample thickness of 2mm ( $\pm$  .5 mm). The mass of the powder compacts was less than .2 grams and the measured sample powder was loaded into the die and compressed statically with a Carver Auto-Series hydraulic press. While the extent of densification can be adjusted based on the pressure applied and amount/type of powder, the goal was to press the powder mixtures to the highest density possible (greater than 90 percent TMD), with the maximum force ranging between 2600-2800lb-force.

### ***3.4 Modified-Taylor Rod-on-Anvil Impact Test Setup***

To conduct the impact-initiation experiments with the 7.62 mm gas gun, a modified rod-on-anvil Taylor test setup was employed using a 7.62 mm diameter and 30 mm long copper 1100 alloy projectile. The projectile (nominal 12 g weight) was mounted with a pressed powder compact on the front and held in the center with a thin layer of epoxy (Fig. 31).



This projectile was then loaded into the breech of the 6 ft barrel, .30 caliber gas gun and accelerated to speeds up to approximately 480 m/s. The impact velocity was measured using a laser beam interrupt set up (Physics Applications, Inc). The transient deformation profile of the compacted pellet and deformed projectile, in addition to reaction initiation based on light emission, was captured using high-speed imaging with the Imacon 200 high-speed camera (Specialized Imaging).

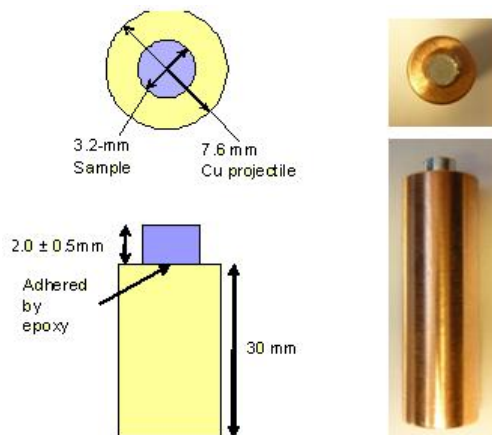


**Figure 31:** Schematic and photograph of sample mounted on a projectile, Left being sample drawing and dimensions and the right being a top and side view of a finished projectile

The schematic of the test setup can be seen in Fig. 32, and an example of high speed camera images revealing reaction light can be seen in Fig. 33. The velocity is obtained when the accelerated projectile interrupts two red laser beams, which trigger a drop in voltage in the inverter box that switches that signal to a rising (positive) pulse. This signal is sent to the up-down counter (Physics Applications). By measuring the distance between each laser, and the distance from the second laser to the rigid anvil, the velocity can be calculated. The camera/flash are also triggered to simultaneously capture the sample and projectile images right before impact to obtain 16 frames of the transient deformation and reaction light emission. The experiment chamber was maintained either with the atmosphere being air or vacuum. When evacuating, the chamber was pumped down to below 50 mTorr. For experiments in air, the chamber was left unsealed and at atmospheric pressure.

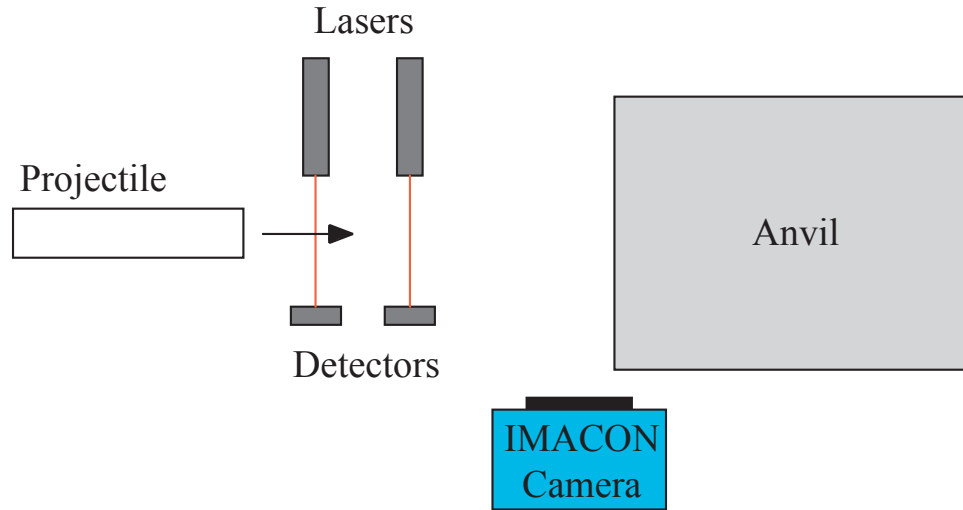


**Figure 32:** Schematic of experimental set up, with projectile, laser beam velocity trap, high-speed camera, and anvil

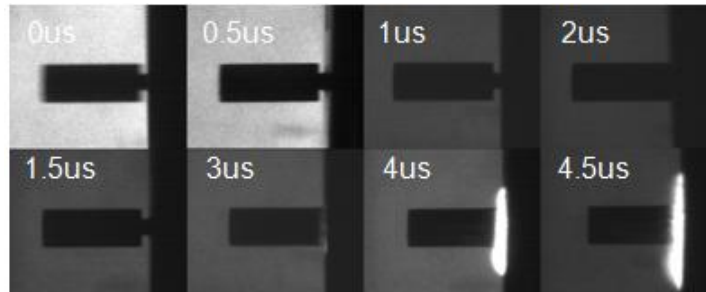


**Figure 33:** Taylor rod-on-anvil impact initiation test in vacuum of Ta-Al equal-vol ratio at a speed of  $\approx 500$  m/s

### ***3.5 Reaction Product Recovery and Characterization***

Recovery of reaction products was carried out using different methods because of the size of the samples used in the experiments which made reaction products difficult to recover. Three different recovery techniques were employed in attempts to recover and characterize reaction products. Initially, XRD was performed on the impact surface of the recovered projectile in order to detect presence of reaction products that may have formed. Another recovery approach involved capturing the material ejecta after impact in a radial polycarbonate hoop. Following impact, the material is ejected radially from the impact surface spraying the debris in a ring. Multiple variations confinements were attempted and were attached to the anvil face around the impact area. The first of these devices was a box made from clear polymethyl methacrylate (PMMA) plastic, with glycerin soap lining to capture materials. The glycerin would subsequently be melted down, and the particles captured in the glycerin would drop to the bottom of the solution, strained out and characterized using XRD.

A polycarbonate tube was also used (as shown in the experimental setup in Fig. 34) and attached to the anvil face. There was no lining used in this set up. The ring of debris (see Fig. 35) deposited on the inside of the tube was scraped, and collected for characterization using XRD. Lastly a projectile with a recessed hole machined into it (Figures 36 and 37) was developed with the intent of capturing reaction products by trapping them between the projectile and anvil thereby, potentially capturing the ejecta for characterization. The projectile cavity was packed by hand, pressing the intermetallic-forming powder mixture into the recessed pocket of the projectile. The powder was packed by adding small amounts of powder into the recessed hole and pressing with a metal rod of about .125" in diameter, then continually adding powder until the level was even with the edge of the projectile. These recessed rounds were fired normally in the impact initiation tests, with the open powder-packed end as the impact face. After experimentation, the sample/projectile remnants were characterized using XRD.

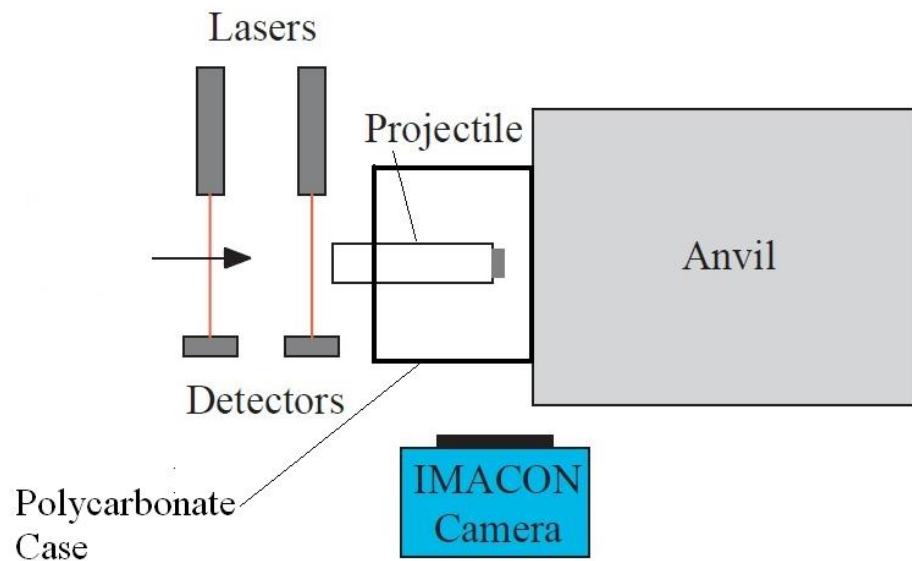


**Figure 34:** Experimental setup with polycarbonate tube for debris capture

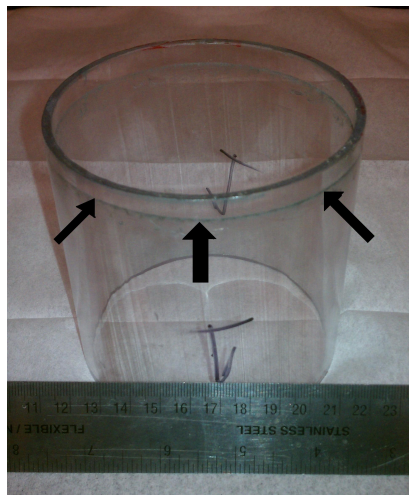


**Figure 35:** Example of polycarbonate tube used in experimentation with "spray" ring of debris

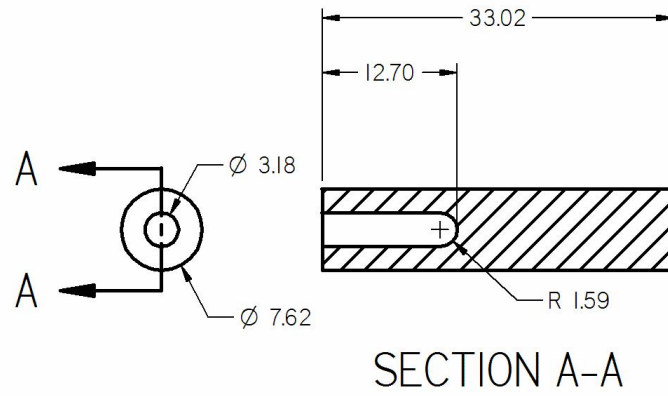


**Figure 36:** Diagram of the recessed round, all measurements are in millimeters

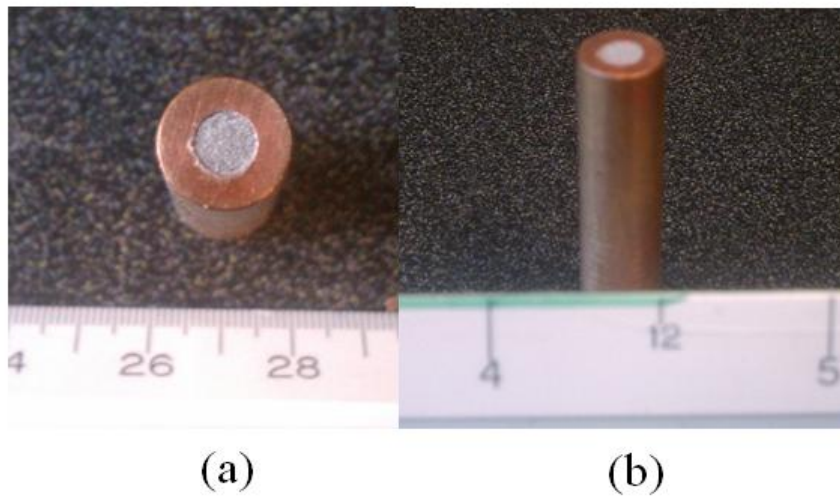


**Figure 37:** Top (a) and side (b) views of filled recessed round

## CHAPTER IV

### RESULTS AND DISCUSSION

The results of the impact experiments performed on each intermetallic-forming mixture and their comparison with pure aluminum are discussed. Experiments on each system, Ta+Al, W+Al, Ni+Al, and Al, were performed individually in both air and vacuum and as a function of compact density. The onset of reaction was deduced based on light emission captured by the camera. The minimum total impact energy resulting in reaction initiation was considered as the total energy dissipated for reaction initiation. Post-experiment analysis of the debris attained from the different recovery experiments was characterized using XRD to determine the type of reaction products formed.

#### *4.1 Intermetallic Systems Overview of Results*

The experimentation for impact initiation of reactions in the various systems was performed in air and vacuum. The sample pellets and projectile characteristics for each system, including the sample density and percent theoretical maximum density (TMD), along with impact velocity and reaction state are listed in Tables 8 to 11.

For each impact experiment, the total kinetic energy ( $KE_T$ ) was determined using Eq.1 where  $m$  is the total mass of the projectile and sample, and  $v_A$  is the actual recorded velocity from the velocity trap during experimentation.

$$KE_T = \frac{1}{2}mv_A^2 \quad (1)$$

The results of all experiments in Tables 8 to 11 are plotted for each reactive material system in Figures 38 to 41, as plots of kinetic energy versus percent theoretical density of the actual powder compact, all for experiments conducted in (a) air or (b) vacuum. In general, Figures 38 to 41 summarize the observed trends based on the total threshold kinetic energy for reaction initiation as follows: (A) Threshold Kinetic energy for reaction

initiation is lower in air than in vacuum for all systems. (B) Only Ta+Al and W+Al show reaction occurring in vacuum, under the range of impact conditions explored, while Ni+Al and Al compacts show no such reaction. (C) In air, Ta+Al reacts with the lowest amount of kinetic energy than all other systems, including Al; with lower density compacts requiring higher energy in air is almost about the same as that for pure Al; Although Ni+Al shows an effect of packing densities while W+Al and pure Al show no obvious effect.

**Table 8:** Sample data of Al experiments and results; part (a) denotes air experiments and part (b) represents vacuum experiments, all with no reaction

Mass w/o Projectile (g)	Mass w/ Projectile (g)	Diameter (cm)	Thickness (cm)	Volume (cm <sup>3</sup> )	Density (g/cm <sup>3</sup> )	Percent Density	Actual Velocity	Environment	Reaction	Kinetic Energy (kJ)	(a)
0.0439	12.1943	0.318	0.2440	0.0194	2.2653	83.9%	407	Air	No	1010	
0.0457	12.2078	0.318	0.2430	0.0193	2.3679	87.7%	406	Air	No	1006	
0.0422	12.2270	0.320	0.2148	0.0173	2.4382	90.3%	407	Air	Yes	1013	
0.0417	12.2497	0.321	0.2100	0.0169	2.4613	91.2%	406	Air	Yes	1010	
0.0434	12.2020	0.320	0.2140	0.0172	2.5217	93.4%	453	Air	yes	1252	
0.0428	12.2540	0.320	0.2101	0.0169	2.5345	93.9%	386	Air	yes	913	
0.0451	12.3990	0.320	0.2191	0.0176	2.5594	94.8%	401	Air	No	997	
0.0528	12.2437	0.320	0.2532	0.0204	2.5929	96.0%	380	Air	No	884	
0.0425	12.2500	0.321	0.1980	0.0160	2.6523	98.2%	453	Air	Yes	1257	
0.0429	12.2408	0.320	0.1992	0.0160	2.6845	99.4%	403	Air	Yes	994	
0.0422	12.2263	0.320	0.1950	0.0157	2.6908	99.7%	476	Air	Yes	1385	

Mass w/o Projectile (g)	Mass w/ Projectile (g)	Diameter (cm)	Thickness (cm)	Volume (cm <sup>3</sup> )	Density (g/cm <sup>3</sup> )	Percent Density	Actual Velocity	Environment	Reaction	Kinetic Energy (kJ)	(b)
0.0426	12.2570	0.323	0.2140	0.0175	2.4294	90.0%	480	Vaccum	No	1412	
0.0419	12.2088	0.321	0.2030	0.0164	2.5505	94.5%	476	Vaccum	No	1383	

**Table 9:** Sample data of Ni+Al experiments and results; part (a) denotes air experiments and part (b) represents vacuum experiments

Mass w/o Projectile (g)	Mass w/ Projectile (g)	Diameter (cm)	Thickness (cm)	Volume (cm <sup>3</sup> )	Density (g/cm <sup>3</sup> )	Percent Density	Actual Velocity	Environment	Reaction	Kinetic Energy (kJ)
0.0873	12.2232	0.319	0.212	0.0169	5.1524	88.8%	354	Air	No	766
0.0673	12.197	0.319	0.162	0.0129	5.1979	89.6%	394	Air	No	947
0.0958	12.1949	0.317	0.233	0.0184	5.2096	89.8%	373	Air	No	848
0.0973	12.2251	0.318	0.235	0.0187	5.2132	89.8%	350	Air	No	749
0.0843	12.196	0.3198	0.2007	0.0161	5.2292	90.1%	328	Air	No	656
0.0793	12.1842	0.3186	0.1892	0.0151	5.2574	90.6%	326	Air	No	649
0.0867	12.2143	0.3190	0.2060	0.0165	5.2660	90.7%	430	Air	No	1129
0.0923	12.232	0.319	0.218	0.0174	5.2975	91.3%	350	Air	No	749
0.0840	12.2543	0.3197	0.1951	0.0157	5.3635	92.4%	469	Air	Yes	1348
0.0858	12.1907	0.3191	0.1948	0.0156	5.5075	94.9%	421	Air	No	1080
0.0839	12.2461	0.3181	0.1908	0.0152	5.5331	95.3%	373	Air	No	852
0.1055	12.2621	0.319	0.238	0.0190	5.5463	95.6%	445	Air	Yes	1214
0.1034	12.2163	0.318	0.234	0.0186	5.5637	95.9%	427	Air	No	1114
0.0833	12.2520	0.3186	0.1878	0.0150	5.5638	95.9%	396	Air	No	961
0.0953	12.2011	0.318	0.215	0.0171	5.5810	96.2%	436	Air	No	1160
0.0847	12.2859	0.3230	0.1810	0.0148	5.7110	98.4%	409	Air	Yes	1028

Mass w/o Projectile (g)	Mass w/ Projectile (g)	Diameter (cm)	Thickness (cm)	Volume (cm <sup>3</sup> )	Density (g/cm <sup>3</sup> )	Percent Density	Actual Velocity	Environment	Reaction	Kinetic Energy (kJ)
0.0830	12.2743	0.3199	0.1925	0.0155	5.3645	92.4%	416	Vacuum	No	1062
0.0830	12.2101	0.3184	0.1883	0.0150	5.5359	95.4%	476	Vacuum	No	1383
0.0844	12.2556	0.3182	0.1914	0.0152	5.5451	95.5%	472	Vacuum	No	1365



**Table 10:** Sample data of Ta+Al experiments and results; part (a) denotes air experiments and part (b) represents vacuum experiments

Mass w/o Projectile (g)	Mass w/ Projectile (g)	Diameter (cm)	Thickness (cm)	Volume (cm <sup>3</sup> )	Density (g/cm <sup>3</sup> )	Percent Density	Actual Velocity	Environment	Reaction	Kinetic Energy (kJ)	(a)
0.1309	12.3999	0.321	0.183	0.0148	8.84	91.2%	413	Air	Yes	1058	
0.1295	12.2580	0.320	0.1812	0.0146	8.89	91.7%	347	Air	No	738	
0.1335	12.2639	0.318	0.1870	0.0149	8.99	92.7%	342	Air	No	717	
0.1295	12.3331	0.321	0.1761	0.0143	9.09	93.7%	407	Air	Yes	1021	
0.1309	12.2884	0.321	0.1776	0.0144	9.11	93.9%	310	Air	No	590	
0.1308	12.3412	0.321	0.1771	0.0143	9.13	94.1%	323	Air	No	644	
0.1437	12.2471	0.318	0.1980	0.0157	9.14	94.3%	336	Air	No	691	
0.1350	12.2993	0.320	0.1838	0.0148	9.14	94.3%	342	Air	No	720	
0.1311	12.2880	0.319	0.1790	0.0143	9.16	94.5%	457	Air	Yes	1283	
0.1320	12.3370	0.319	0.1800	0.0144	9.18	94.6%	336	Air	No	696	
0.1308	12.3420	0.319	0.1780	0.0142	9.19	94.8%	459	Air	No	1300	
0.1220	12.2846	0.318	0.1670	0.0133	9.20	94.9%	356	Air	No	778	
0.1306	12.3568	0.321	0.1754	0.0142	9.20	94.9%	349	Air	Yes	753	
0.1320	12.3430	0.319	0.1780	0.0142	9.28	95.7%	341	Air	Yes	718	
0.1470	12.3380	0.320	0.1980	0.0159	9.23	95.2%	337	Air	No	701	

Mass w/o Projectile (g)	Mass w/ Projectile (g)	Diameter (cm)	Thickness (cm)	Volume (cm <sup>3</sup> )	Density (g/cm <sup>3</sup> )	Percent Density	Actual Velocity	Environment	Reaction	Kinetic Energy (kJ)	(b)
0.1360	12.3091	0.318	0.2022	0.0161	8.47	87.4%	474	Vacuum	Yes	1383	
0.1381	12.2637	0.319	0.1970	0.0157	8.77	90.5%	421	Vacuum	No	1087	
0.1305	12.3620	0.320	0.1820	0.0146	8.92	92.0%	382	Vacuum	Yes	902	
0.1287	12.3208	0.323	0.1750	0.0143	8.98	92.6%	418	Vacuum	No	1076	
0.1299	12.2602	0.321	0.1780	0.0144	9.02	93.0%	412	Vacuum	Yes	1041	
0.1299	12.3005	0.320	0.1790	0.0144	9.02	93.1%	355	Vacuum	No	775	
0.1405	12.3499	0.320	0.1930	0.0155	9.05	93.4%	376	Vacuum	Yes	873	
0.1294	12.3293	0.319	0.1782	0.0143	9.07	93.5%	367	Vacuum	No	830	
0.1162	12.3209	0.321	0.1580	0.0128	9.09	93.7%	353	Vacuum	No	768	
0.1203	12.2775	0.321	0.1620	0.0131	9.18	94.6%	375	Vacuum	Yes	863	

**Table 11:** Sample data of W+Al experiments and results; part (a) denotes air experiments and part (b) represents vacuum experiments

Mass w/o Projectile (g)	Mass w/ Projectile (g)	Diameter (cm)	Thickness (cm)	Volume (cm <sup>3</sup> )	Density (g/cm <sup>3</sup> )	Percent Density	Actual Velocity	Environment	Reaction	Kinetic Energy (kJ)
0.1639	12.331	0.32	0.198	0.0159	10.29	93.3%	465.82	Air	Yes	1338
0.167	12.342	0.319	0.199	0.0160	10.45	94.7%	401	Air	Yes	991
0.169	12.319	0.319	0.200	0.0160	10.58	96.0%	384	Air	No	909
0.167	12.325	0.319	0.197	0.0158	10.60	96.1%	406	Air	Yes	1015
0.167	12.345	0.319	0.197	0.0158	10.61	96.2%	402	Air	Yes	997
0.169	12.306	0.319	0.198	0.0159	10.67	96.7%	482	Air	Yes	1429
0.167	12.326	0.319	0.194	0.0156	10.70	97.0%	350	Air	No	754
0.169	12.353	0.319	0.197	0.0157	10.75	97.5%	439	Air	Yes	1189
0.168	12.439	0.319	0.195	0.0156	10.77	97.6%	390	Air	Yes	945

(a)

Mass w/o Projectile (g)	Mass w/ Projectile (g)	Diameter (cm)	Thickness (cm)	Volume (cm <sup>3</sup> )	Density (g/cm <sup>3</sup> )	Percent Density	Actual Velocity	Environment	Reaction	Kinetic Energy (kJ)
0.1659	12.3282	0.319	0.2	0.0160	10.38	94.1%	434	Vacuum	No	1161
0.176	12.3075	0.32	0.2108	0.0170	10.38	94.1%	427	Vacuum	No	1122
0.1653	12.2807	0.319	0.199	0.0159	10.39	94.2%	478.96	Vacuum	Yes	1409
0.166	12.292	0.319	0.199	0.0159	10.40	94.3%	463	Vacuum	Yes	1318
0.1642	12.3491	0.32	0.196	0.0158	10.42	94.4%	453.09	Vacuum	Yes	1268
0.1681	12.285	0.319	0.2	0.0160	10.52	95.3%	444	Vacuum	Yes	1211
0.1683	12.294	0.32	0.197	0.0158	10.62	96.3%	469	Vacuum	No	1352
0.168	12.359	0.319	0.197	0.0157	10.68	96.9%	487	Vacuum	Yes	1468
0.168	12.370	0.319	0.194	0.0155	10.81	98.0%	411	Vacuum	No	1047
0.164	12.337	0.319	0.189	0.0151	10.83	98.2%	449	Vacuum	No	1244

(b)

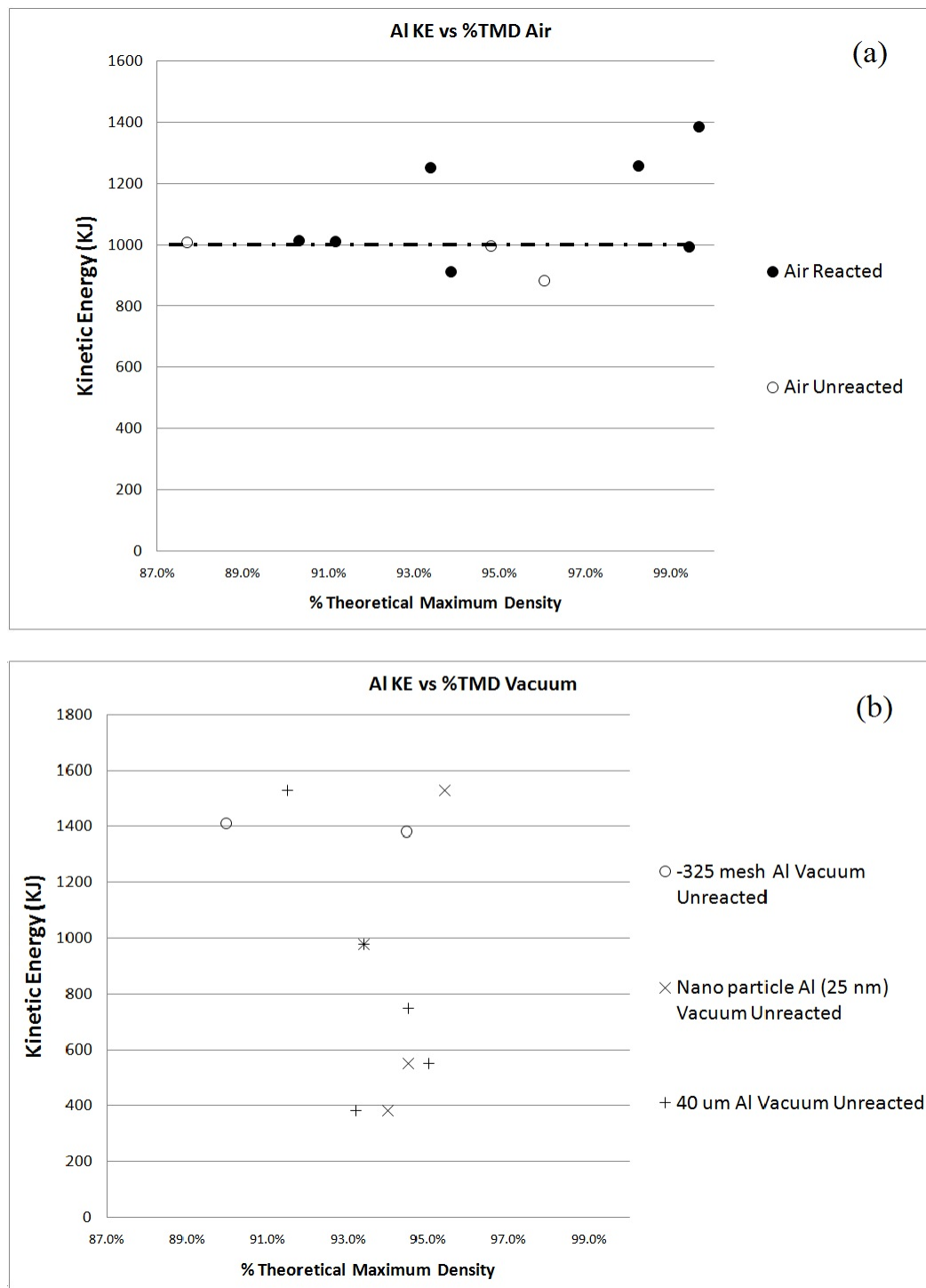


**Figure 38:** Sample data of Al experiments and results; (a) denotes air and (b) represents vacuum. \*Nanoparticle and 40 micron data points were provided from the work of Dr. Seiwei Du.

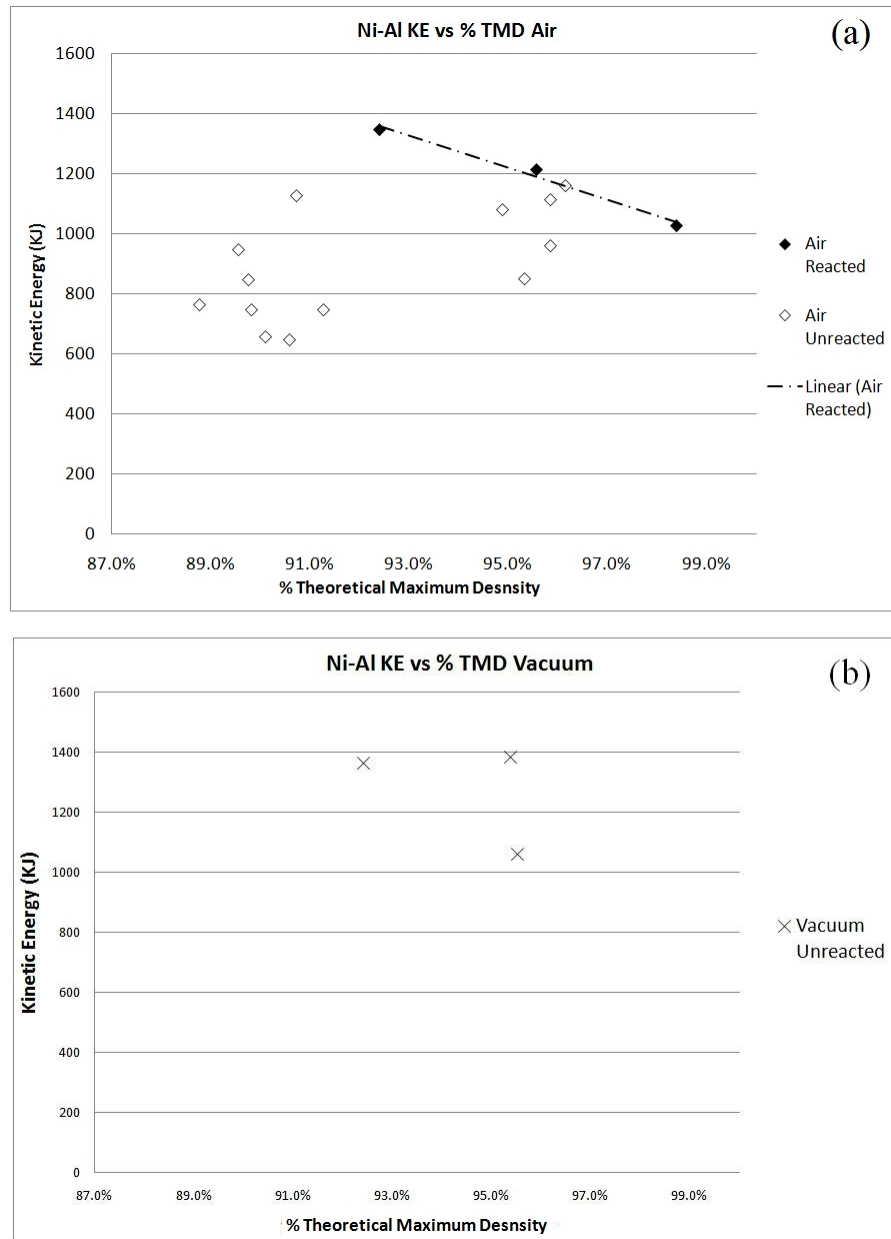


**Figure 39:** Sample data of Ni+Al experiments and results; (a)denotes air and (b) represents vacuum.

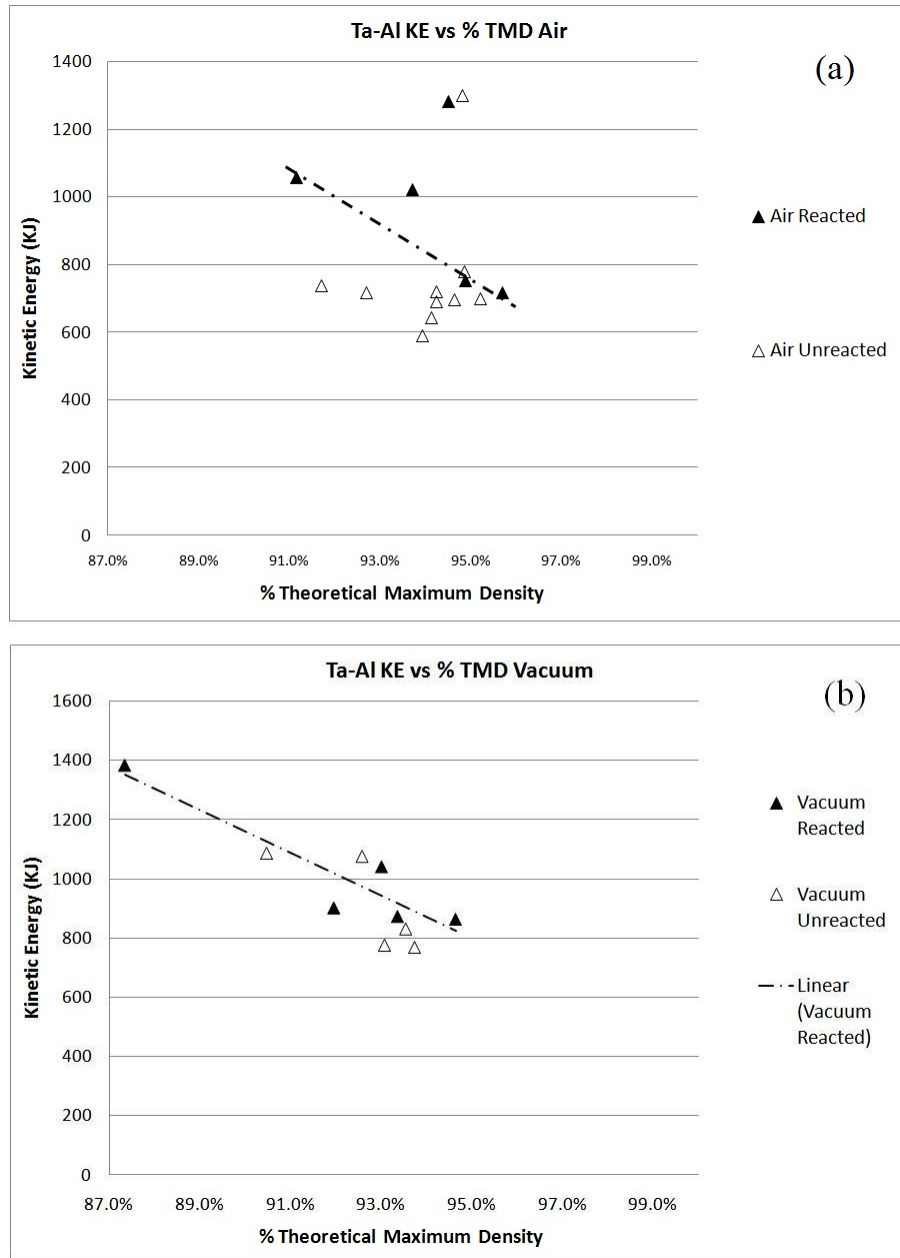


**Figure 40:** Sample data of Ta+Al experiments and results; (a)denotes air and (b) represents vacuum.

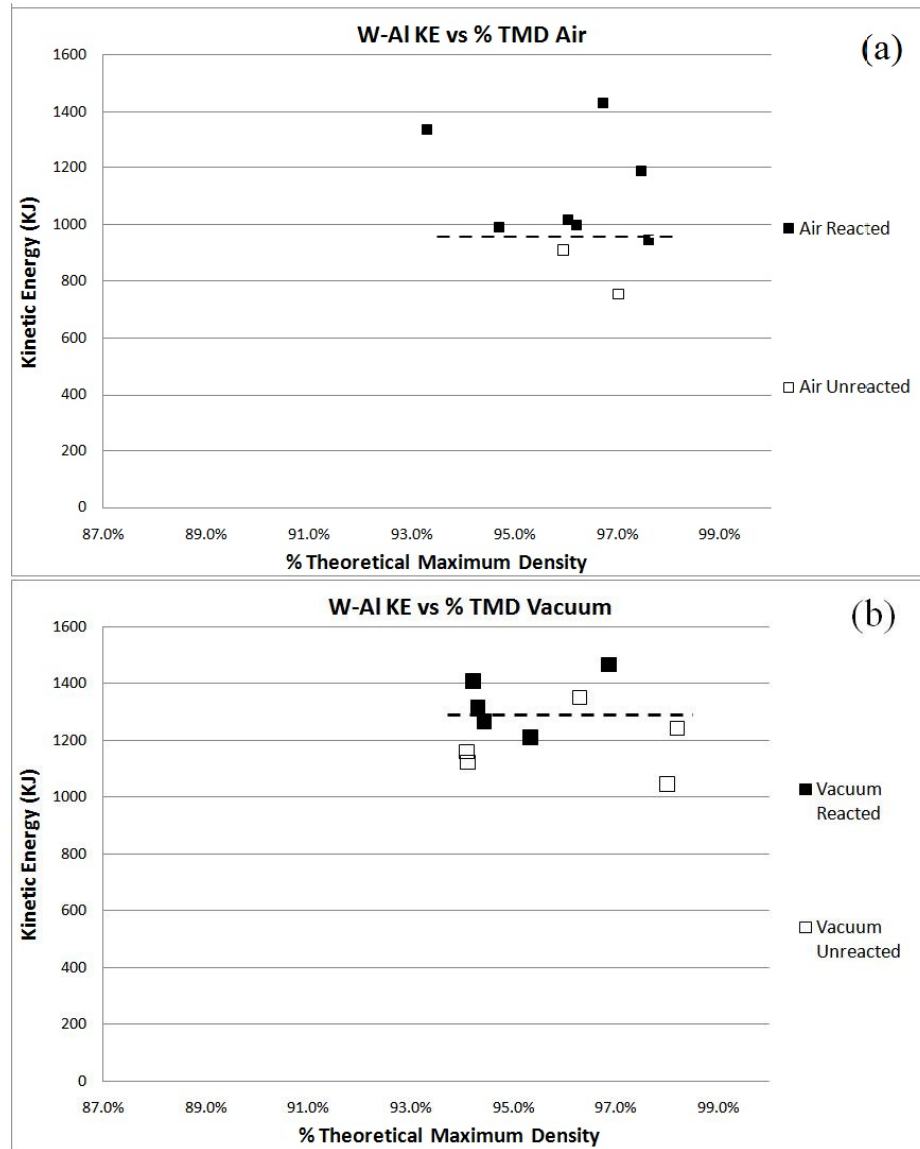


**Figure 41:** Sample data of W+Al experiments and results; (a)denotes air and (b) represents vacuum.

In the case of pure Al powder compacts (Fig. 38 (a) and (b)), while no reaction is observed in vacuum for the range of compact densities and impact conditions studied, the combustion (oxidation) reaction in air appears to be independant of the compact densities ranging from 87 to 99 percent TMD. The Ni+Al mixtures (Fig. 39) show no reaction in vacuum. However reactions in air appear to be dependent on the packing density of the compacts, with 99 percent dense compacts reacting at a lower threshold than lower density compacts. The Ta+Al compacts (Fig. 40), show reaction initiation in both air

and vacuum, with the threshold energy being lower in air than in vacuum. The trend of decreasing reaction energy with increasing compact densities is also observed in Ta+Al, both in air and vacuum. The W+Al compacts (Fig. 41) also show reaction initiation both in air and vacuum with the threshold energy being lower in air. However the effect of compact density is not so obvious in this system. In a study done by Herbold, et al [41], experiments on rods of AL/PTFE fired in both air and vacuum environments, the reaction was “twice as fast” in air when comparing the same reaction in vacuum, indicating that they are aerobic reactions.

The combined results plotting kinetic energy as a function of system density for all reactive materials is shown in Fig. 42 for experiments performed in (a) air and (b) vacuum. The graph shows the reactivity of each material system as a whole (in both air and vacuum) as compared to the other systems. The trend lines representing lowest threshold conditions indicate the higher reactivity of Ta+Al in both air and vacuum. The lowest threshold conditions for reaction initiation are listed in Table 12.

**Table 12:** Lowest threshold conditions for reaction initiation for each intermetallic system in (a) air and (b) vacuum for a nominal density of 94 - 97 percent TMD

Intermetallic System	Environment	Percent TMD	Actual Velocity (m/s)	Reaction	Kinetic Energy (KJ)	(a)
Ta-Al	Air	95.7%	341	Yes	718	
W-Al	Air	97.6%	390	Yes	945	
Ni-Al	Air	95.6%	445	Yes	1214	
Al	Air	93.9%	386	Yes	913	

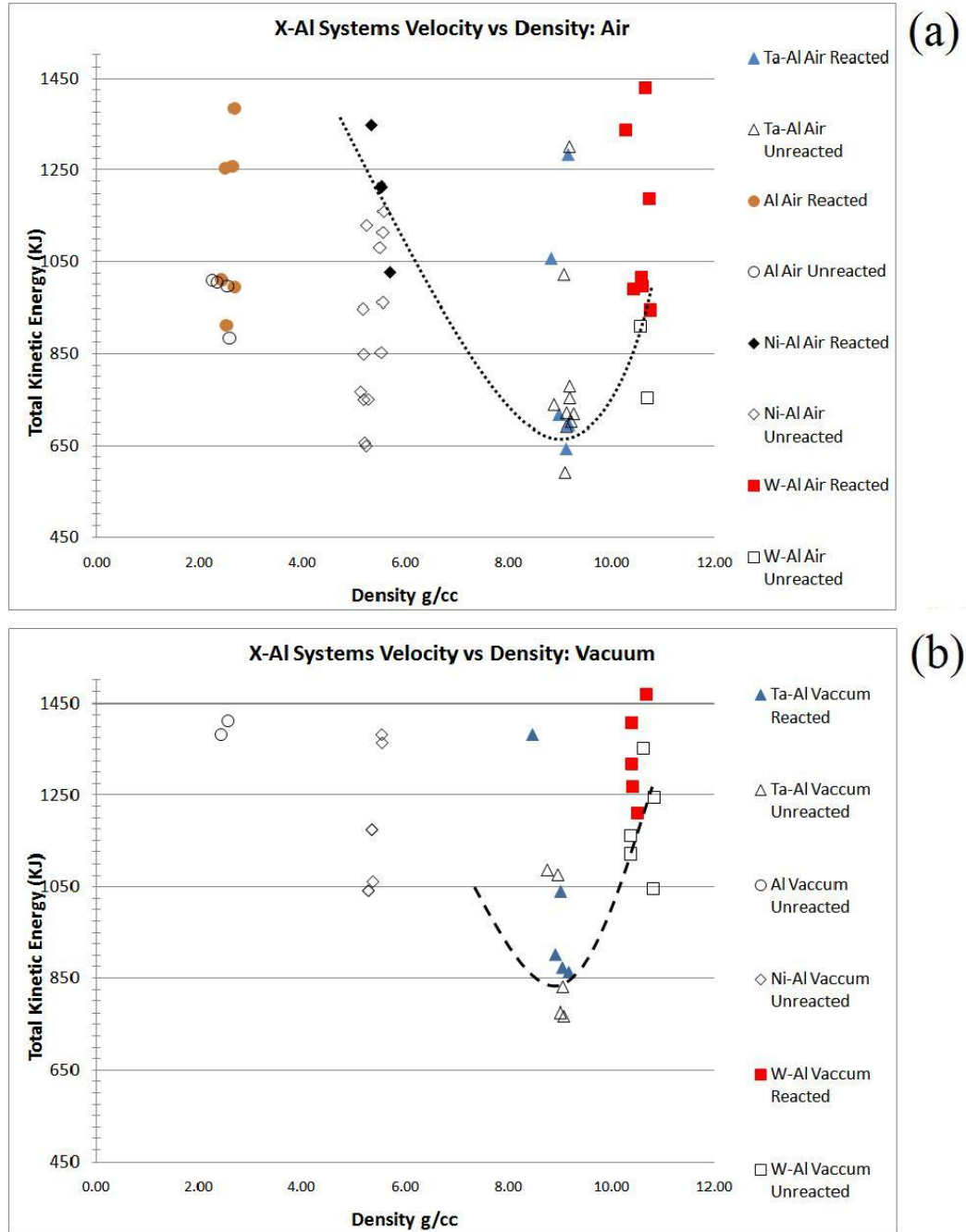
  

Intermetallic System	Environment	Percent TMD	Actual Velocity (m/s)	Reaction	Kinetic Energy (KJ)	(b)
Ta-Al	Vacuum	94.6%	375	Yes	863	
W-Al	Vacuum	95.3%	444	Yes	1211	

The total energy for reaction initiation is directly associated with the total KE involved at impact, when reaction occurs. However, the KE during impact is not fully used in reaction

initiation. To further specify the energy necessary in initiating a reaction, the energy dissipated in the deformation of the sample should be examined, since it is the plastic deformation energy that would be involved in initiating a reaction in any of these systems.

In the speed and scale of these experiments, where deformation and reaction occur on the



**Figure 42:** Graph of experimental data points by system plotted by the Kinetic Energy verses sample density in (a) air and (b) vacuum.



order of microseconds, determining the exact energy involved in impact initiated reaction is difficult without proper instrumentation. Conceptually, the energy input for deformation is the total available kinetic energy, but only a small portion of that is used for reaction. That portion is the energy necessary to cause the plastic deformation in the sample, creating the necessary shear and strain in the compact for reaction. Therefore, the actual (plastic) energy can be determined from the difference between the initial velocity and velocity at reaction.

With the images of the impact event recorded during experimentation, the reaction is captured in frames revealing light emission. The decelerated velocity of the sample at reaction following impact can be calculated in reference to the distance traveled in comparison to other images captured during the event and the reference distances from projectile measurements. Those distances allow for the calibration of a fixed unit of measure for each pixel and since the frames are timed, the distance and time between frames provide a measure of velocity.

Hence, the velocity at reaction can be used to calculate the  $KE_D$  or energy dissipated in the reaction initiation process or that is actually used in deformation leading to reaction initiation. Equations 2 and 3 were used to determine the plastic energy dissipated at the onset reaction and actual plastic energy to cause reaction initiation where,  $KE_A$ ,  $m$  is the mass of the projectile and sample,  $v_T$  is the initial velocity recorded, and  $v_R$  is the velocity at reaction. For  $v_R$ , the imaging software, SIM Control from Specialized Imaging, was used.

$$KE_D = \frac{1}{2}mv_R^2 \quad (2)$$

$$KE_A = \frac{1}{2}m(v_T - v_R)^2 \quad (3)$$

In attaining the  $v_R$  velocity, a point is taken in a frame on one of the eight camera channels (that corresponds to the reaction frame) at one of the projectile's back corners. In the second (reaction) frame, a point is selected on the same corner as in the first frame. The program calculates the velocity instantaneously based on the pixel position of the

point selected. Depending on the resolution of the images the variation between pixels could result in a larger difference in velocity. In Table 13, the actual velocity range of the pixel at reaction in each system for both a horizontal and vertical shift in velocity are listed. The velocity at reaction and pixel range/tolerance for both horizontal and vertical measurements were determined with the camera operating software, SIM control.

The estimated actual velocity is more than likely an upper bound estimation in the energy necessary for reaction. There is not an accurate way to estimate the amount of strain in the copper projectile once it fully deforms the sample pellet and begins to deform itself before reaction. The energy can then be calculated from that strain to provide a more accurate actual energy in deformation. The exact time of reaction initiation may also be unseen due to the limited view of only one side of the cylindrical pellet, or the initiation may even occur in between frames. The large scatter in data due to these limitations makes it difficult to determine the influence of various effects on the actual energy threshold for reaction initiation. Thus, the specific kinetic energy (SKE) was determined on the basis of the total kinetic energy  $KE_T$  instead of the  $KE_D$  at the onset of reaction, and is divided by the mass of the sample  $m$  given in equation 4.

$$SKE = \frac{KE_T}{m} \quad (4)$$

The threshold energy density (ED) was also determined based on the calculation used by Spey [13], and given by Equation (Eq. 5) where  $KE_T$  is the total kinetic energy, and  $V$  represents the volume of the sample.

$$ED = \frac{KE_T}{V} \quad (5)$$

These equations provide a relation that involves the total energy necessary to initiate reaction while normalizing with the density for each system, thereby allowing for an even comparison of the energy necessary from both a mass and volumetric consideration. Table 13 lists the threshold total and specific energy, and the energy density for reaction initiation for each material system. The maximum and minimum actual energy estimate from the pixel range, for calculation of specific KE and energy density are also listed.

**Table 13:** Lowest Values for each equi-volumetric system of experimentally recorded velocity, velocity determined at reaction, and horizontal and vertical range and tolerances per pixel and calculated actual initiation energy Eq.3 , energy dissipated in reaction Eq. 2, actual specific kinetic energy Eq. 4, and energy density Eq. 5 and minimum and maximum actual kinetic energy determined from pixel ranges at reaction per system

	Percent TMD	Actual Velocity	Atm	KE_T (KJ)	Velocity at Reaction	Horizontal Range (m/s)	Vertical Range (m/s)	KE_D (KJ)	KE_A (KJ)	Min KE_A (KJ)	Max KE_A (KJ)	SKE (KJ/g)	ED (KJ/cm <sup>3</sup> )
Ta-Al	95.7%	341	Air	718	334.57	329.92 - 339.21	334.54 - 334.57	687	0.255	0.02	0.75	5437	49883
	94.6%	375	Vac	863	365.80	360.47 - 371.14	365.37 - 366.31	821	0.520	0.09	1.30	6615	58977
W-Al	97.6%	390	Air	945	381.14	375.15 - 387.24	381.05 - 381.43	903	0.460	0.04	1.32	5623	60556
	95.3%	444	Vac	1211	435.07	431.16 - 438.99	434.98 - 435.20	1163	0.490	0.16	1.03	7204	75761
Ni-Al	95.6%	445	Air	1214	438.10	433.55 - 442.66	437.89 - 438.37	1178	0.292	0.03	0.81	11507	63822
Al	93.9%	386	Air	913	372.74	368.83 - 380.56	376.47 - 376.88	853	1.077	0.18	1.81	21329	54060

## 4.2 Comparison of Reaction Initiation Energy Thresholds

### 4.2.1 Effect of Environment: Air Versus Vacuum

In examining the threshold energies from Table 12 the most resounding difference between air and vacuum is that all the systems were able to react within an ambient air atmosphere. Ni+Al and pure Al were both unable to react in vacuum at the maximum capabilities that the .30 caliber gas gun could provide. This observation indicates that oxidation reactions are more prevalent in causing a reaction in Ni+Al and pure Al systems.

In the case of Ta+Al and W+Al, the reaction threshold drops respectively by 34 m/s (145 kJ) and 73 m/s (973 kJ), between reaction initiation in air and vacuum, indicating that there is a combination of oxidation and anaerobic reaction. In vacuum environment, the reaction in W+Al and Ta+Al maybe primarily occurring as an intermetallic-forming or anaerobic event. In air, it is possible that the anaerobic reaction sustains the oxidation reaction with even lower energy thresholds.

### 4.2.2 Material System Density Effects

From the perspective of reactivity, the more dense systems of W+Al and Ta+Al were the most reactive since they reacted in both the air and vacuum environments. The Ta+Al

mixture has a theoretical density of  $9.695 \frac{g}{cm^3}$  and its reaction threshold in air and vacuum was lower than W+Al which has a theoretical density of  $11.03 \frac{g}{cm^3}$ . Additionally, threshold for W+Al was higher than for pure Al at  $2.7 \frac{g}{cm^3}$  in air but lower in vacuum. Threshold energy of Al in air is lower than every other system except Ta+Al in which case the reaction is dominated by anaerobic mechanisms. Hence, while density is an important aspect of how these materials are combined, the material strength may also effect the outcome in terms of the reaction initiation because of its influence on deformation of combustion. The difference in reactants between Ta+Al and W+Al is plausibly due to the effect of strength differences, since Ta is more ductile than W.

The packing density (percent TMD) also affects how and if a system is reactive or not. In a study done by Herbold et al [41], on two ball milled samples of equal atomic stoichiometry Ni+Al, it was observed that higher packing density samples systems (95 percent TMD) had a lower threshold for reaction initiation than the lower packed density sample systems. As shown in Fig. 43 from Herbold et al's study [41], a trend can be seen in the energy required to react. Herbold et al's findings can also be corroborated by data obtained in the present work on Ni-Al samples at densities in the range of 89 - 99 percent TMD, as shown in Fig. 39 (a). It can be seen that samples of higher densities (greater than 90 percent TMD) react where those close to 90 percent show no reaction in the impact velocity range of 403 - 407 m/s. The Ta+Al system also shows a similar trend with denser compacts having a lower reaction energy threshold, both in air and vacuum, as show in Fig. 40 (a,b). The effect of packing densities in the case of W+Al is less obvious.

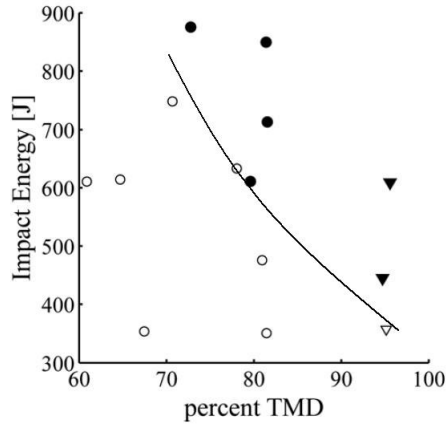


**Figure 43:** The kinetic energy of the Cu sabot and pellet is plotted as a function of percent TMD of the Ni+Al pellet. The open markers (open circle for SARM1 and open triangle for SARM2) indicate no reaction. The closed markers indicate a distinct reaction before the sabot [projectile] hits the anvil. The impact energy threshold for SARM1 and SARM2 milled to 35 percent of the averaged time to milling reaction, decreases for increasing pellet density. Taken from [41]

#### 4.2.3 Particle Size Effects

The particle size of the material system can also have an effect on reactivity and sample densification. In Fig. 44 a plot of percent TMD vs KE is shown for equi-volume Ni+Al in both -325 mesh and +325 -200 mesh samples of Ni in the equi-volumetric experimental data. The data points for the coarser particles are of a lower density but still have some overlap with the low density results for the -325 mesh powder mixture experiments. From Fig. 44, it can be seen that while the effect of packing density on reaction initiation threshold is observed for both sizes of powder mixtures; the coarser mixture (+325 -200 mesh) has a lower reaction energy threshold than the finer (-325 mesh) Ni+Al mixture. In fact, the coarser Ni+Al reacts at lower energy than the pure Al, which suggests that the higher degree of stress and strain in coarser particles makes them react at lower energies and lower compact densities. Coarser particles provide more enhanced strain localization due to fewer inter-particle contact points and consequently higher strain.

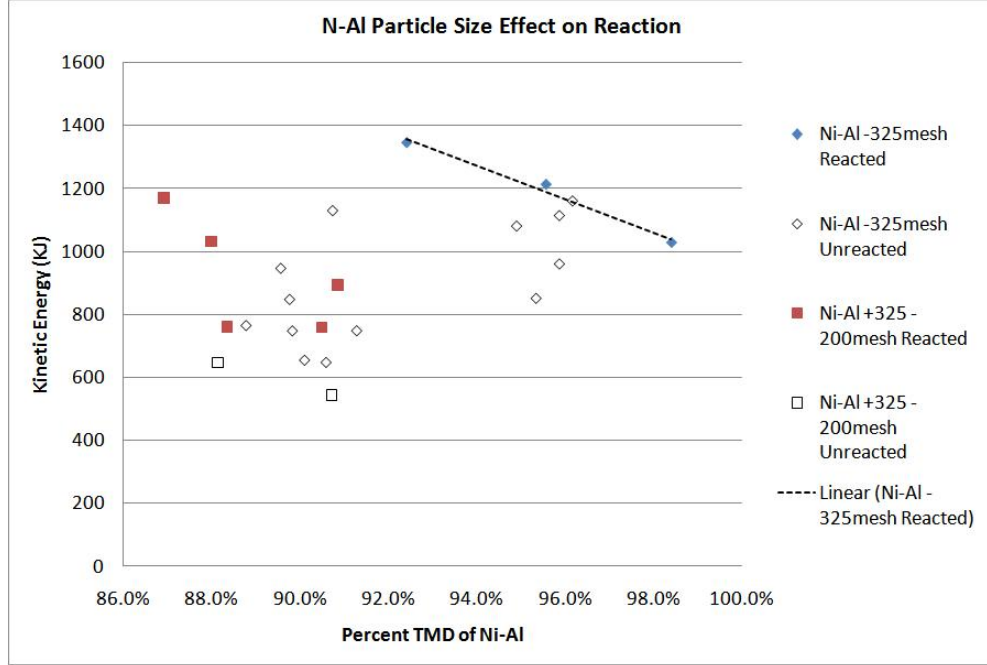


**Figure 44:** Figure showing labeled points of percent TMD verses KE, for Ni-Al differing in particle sizes of -325 Mesh and +325 -200 mesh

#### 4.2.4 Material System Strength Effects

Recently, the effects of strength difference between reactants in Ni+Al, W+Al, and Ta+Al, has been investigated using mesoscale numerical simulation by Aydelotte and Thadhani [3]. In this study, microstructures of the previously mentioned equi-volumetric, shock-compacted reactive materials were developed from actual samples and image processed into a multi-material Eulerian hydrocode simulation program called CTH and compared with experimental results, which indicate that Ta+Al reacted at a much lower specific kinetic energy than Ni+Al and W+Al. With the use of CTH simulation, it was observed that both constituents of the Ta+Al system underwent more plastic strain on average than the Ni+Al and W+Al mixtures (even though the maximum value for strain in Ta+Al was approximately the same as Ni+Al). The strain produced by Ta+Al adds adiabatic heating leading to reaction initiation. Although, Ni+Al has a lower yield, it strain-hardens considerably, making its strength higher than that of Ta+Al, reducing the amount of strain, and making it less reactive than Ta+Al. In the case of W+Al, with the high yield strength of W, it strained only about 5 percent, making it more difficult to react than Ta+Al.

### ***4.3 Recovery Experiments and Characterization***

The following sections display the characterization attempts through XRD for each system for both the polycarbonate surrounding ring experiments and recessed round projectiles for the various intermetallic-forming systems investigated.

#### **4.3.1 Polycarbonate Ring Experimental Results**

The sample ejecta was captured by the polycarbonate ring, scraped, and characterized with XRD. In Figures 45 to 48 are the XRD traces resulting from these scans. Each peak is identified by the material composition. The initial amorphous “hump” at the  $2\theta$ , 20 degree position is the peak corresponding to the polycarbonate pieces intermixed with the sample debris being scanned. The figures show that the debris reveals no evidence of reaction products (either due to oxidation,  $\text{Al}_2\text{O}_3$  is located in the 35 deg area, or intermetallic-forming) since each peak is identified in its elementary form (either the X-material or Al). The lack of presence of reaction product could be due to one or some combination of:

- The very small sample size used during experimentation,
- When reaction occurs the reaction products are vaporized during the process,
- Or the location of the polycarbonate could not be in the optimal position to capture these products.

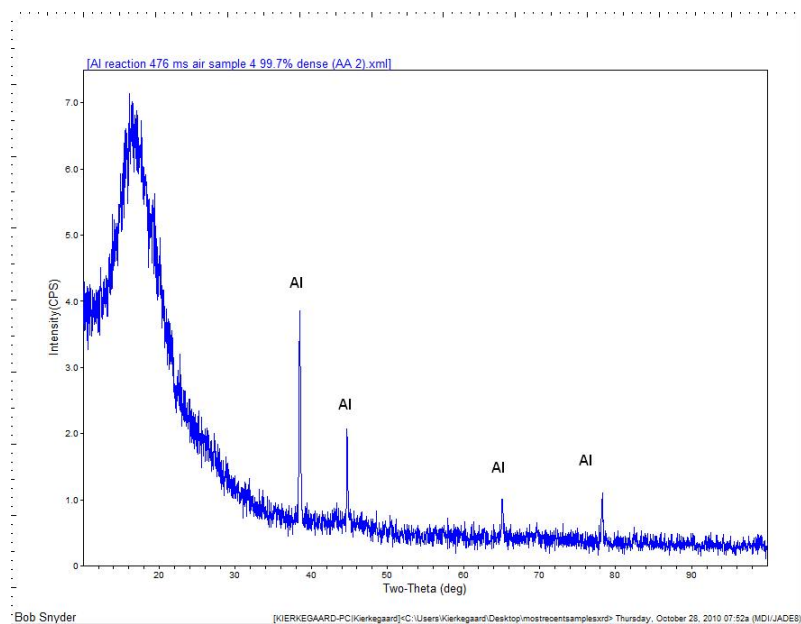


**Figure 45:** XRD trace of experimentally reacted Al fired at 476 m/s in air with at 99.7 percent TMD with no reaction products

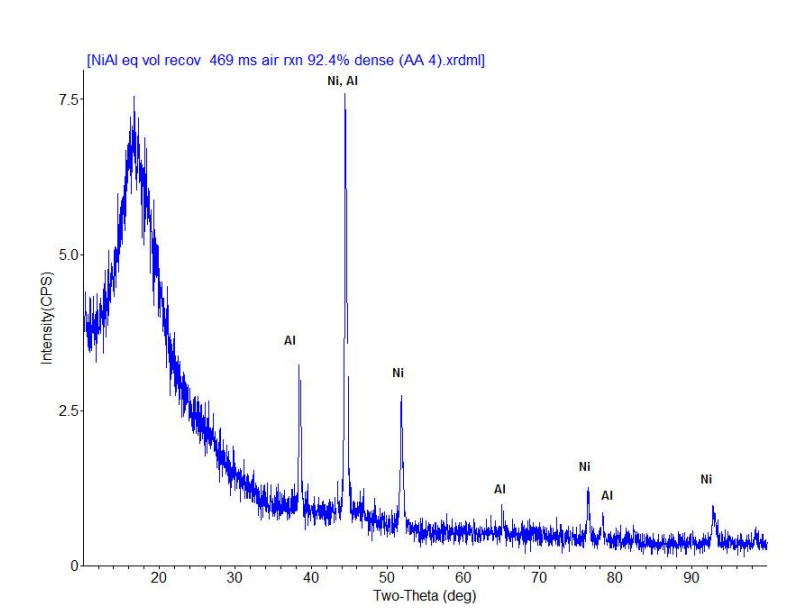


**Figure 46:** XRD trace of reacted equi-volume mix of Ni+Al at 469m/s in air at 92.4 percent TMD with no reaction products



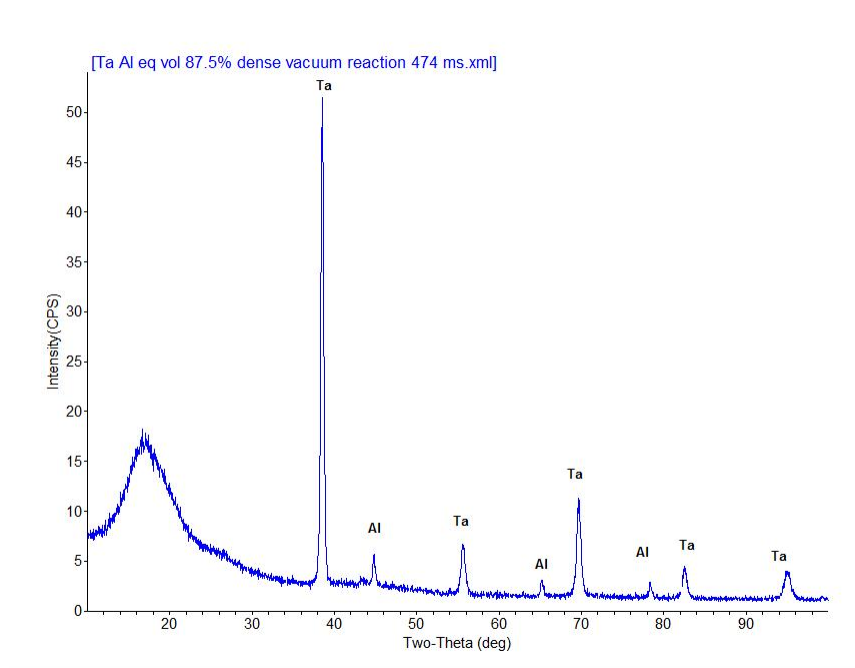


**Figure 47:** XRD trace of reacted equi-volume mix of Ta+Al at 474m/s in vacuum at 87.4 percent TMD with no reaction products

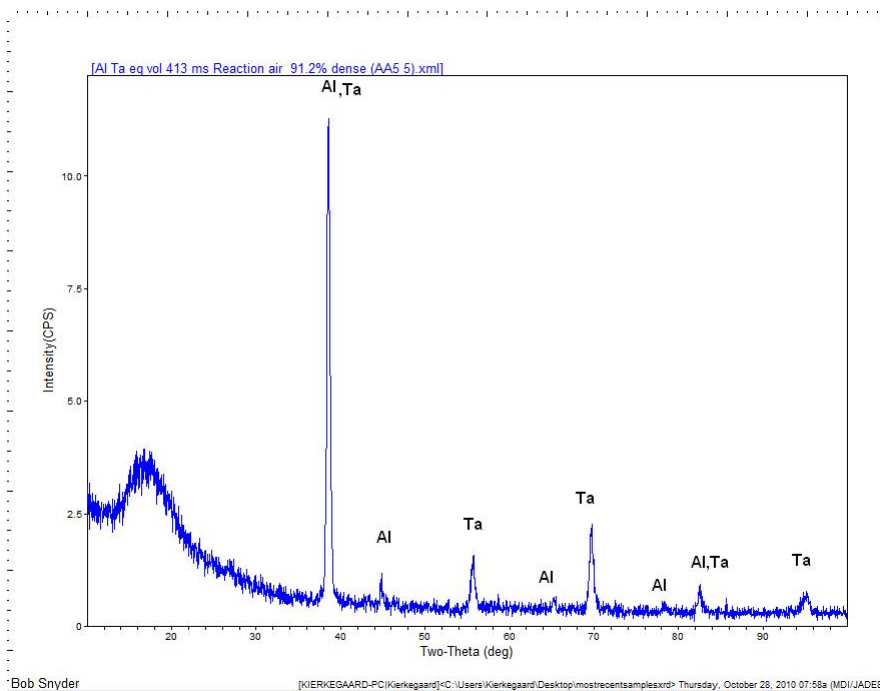


**Figure 48:** XRD trace of reacted equi-volume mix of Ta+Al in air at 413m/s at 91.2 percent TMD with no reaction products

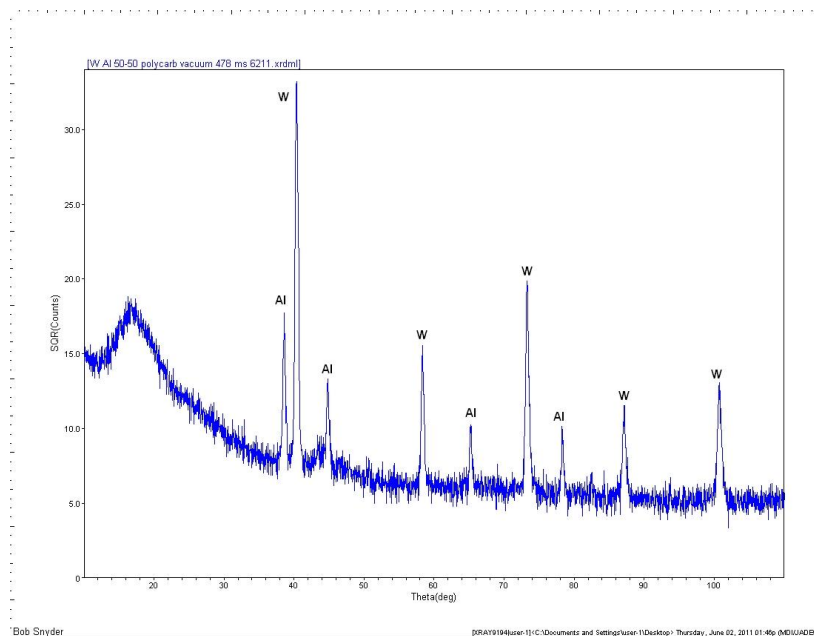


**Figure 49:** XRD trace of reacted equi-volume mix of W+Al in vacuum at 478m/s at 94.1 percent TMD with no reaction products. The unidentified peaks at approximately 42 and 43 deg belong to Cu and possibly  $\text{Al}_2\text{Cu}_3$

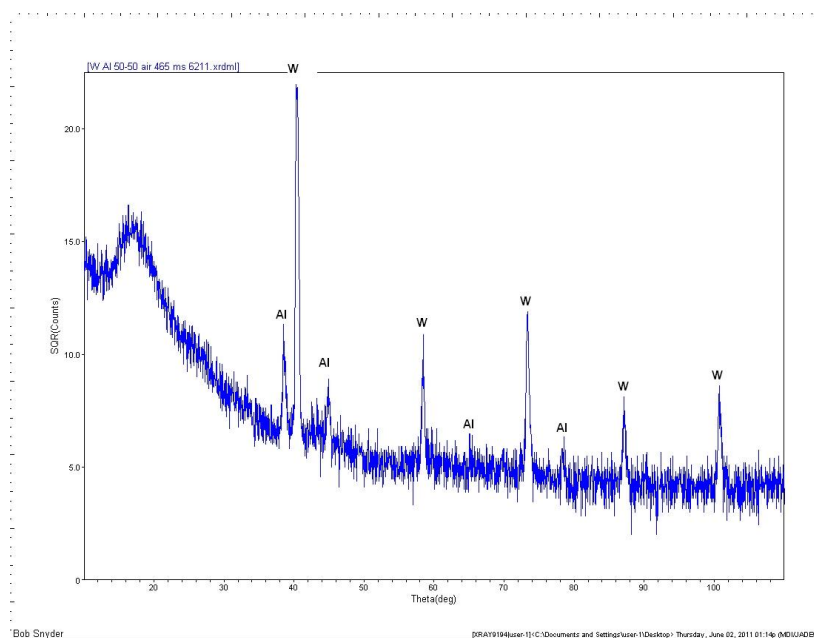


**Figure 50:** XRD trace of reacted equi-volume mix of W+Al in air at 465m/s at 93.3 percent TMD with no reaction products

### 4.3.2 Recessed Projectile Experimental Results

The recessed projectile experiments were used to impact the anvil at the highest velocity attainable ( $\approx 480$  m/s) for that experimental setup. After impact, the projectile debris was collected from the experimental chamber and then characterized using XRD. Figures 51 to 54 show the XRD traces of the recessed projectile experiments. Because of the geometry of the experiment and projectile, it was not possible to see reaction light; therefore, XRD characterization was the only way to determine if a reaction occurred.

The recessed projectiles showed no evidence of reaction with all peaks being accounted for in both Cu and Al locations as shown in Fig. 51 for Al, and in Fig. 52 for Ni+Al, major peaks accounted for with either Ni, Al, or Cu. However there are undefined peaks located in the 43-45 degree  $2\theta$  range. Likewise, Fig. 53 shows no evidence of reaction in W+Al with all peaks accounted for in either W or Cu. In the case of these scans, Al peaks are not seen due to the characteristics of the other materials scanned during XRD, forcing the Al to have smaller peaks or completely drowned out by the intensity of the W or Cu from the projectiles. It is also possible that the oxidation of Al and the vaporization of  $\text{Al}_2\text{O}_3$  would inhibit observation of reaction product peaks. The only conclusive XRD scan indicating the presence of reaction products was for Ta+Al as show in Fig. 54. There were two experiments performed in air at velocities of 357 m/s and 483 m/s parts (a) and (b) respectively, of which both resulted in intermetallic reaction products forming  $\text{Ta}_3\text{Al}_2$  and  $\text{TaAl}_3$ . This result provides further credence to the occurrence of anaerobic reaction in Ta+Al in both air and vacuum environment

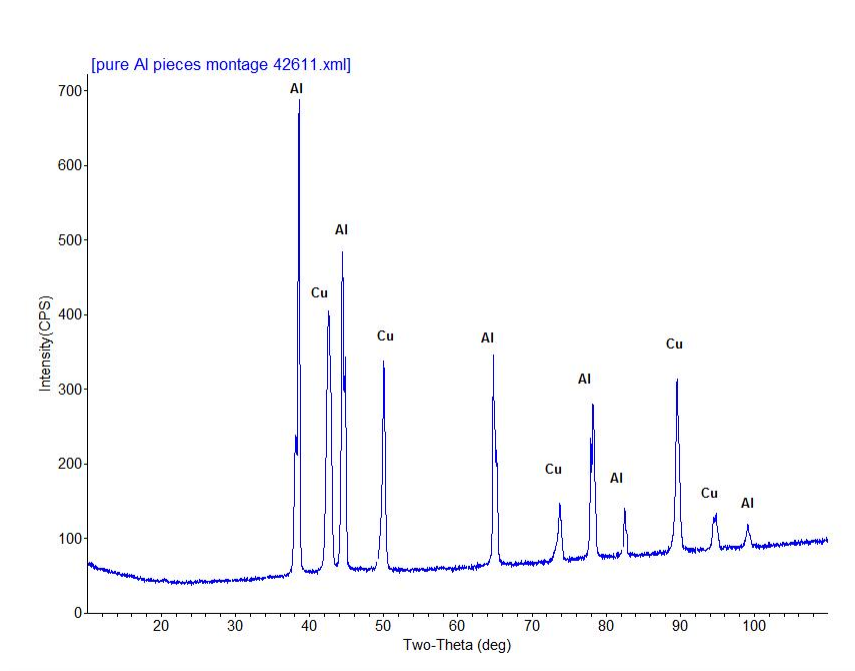


**Figure 51:** XRD trace of recessed projectile packed with pure Al fired at maximum velocity  $\approx 480\text{m/s}$  in air

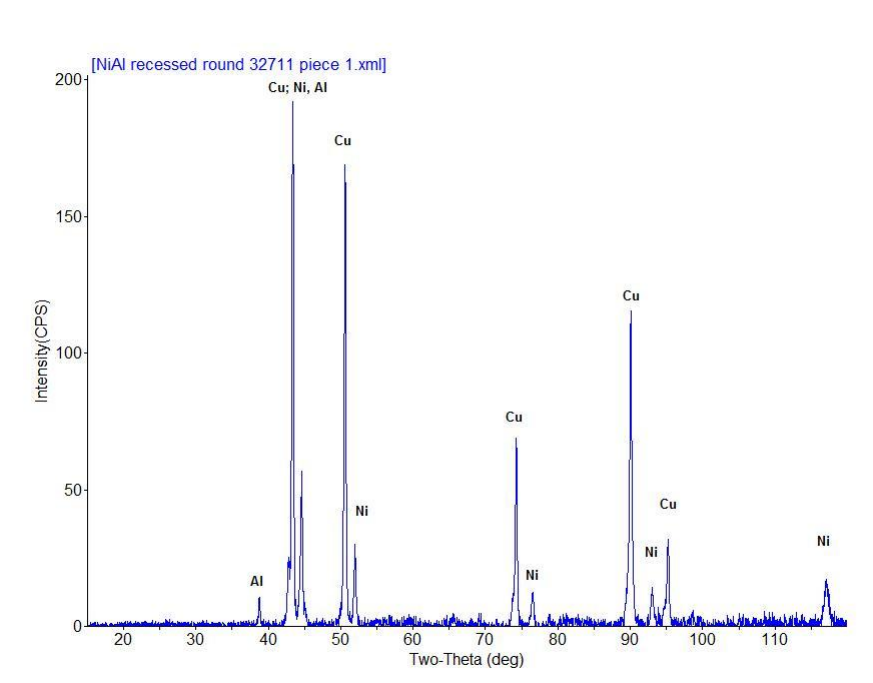


**Figure 52:** XRD trace of recessed projectile packed with equi-volume mix of Ni+Al fired at maximum velocity  $\approx 480\text{m/s}$  in air

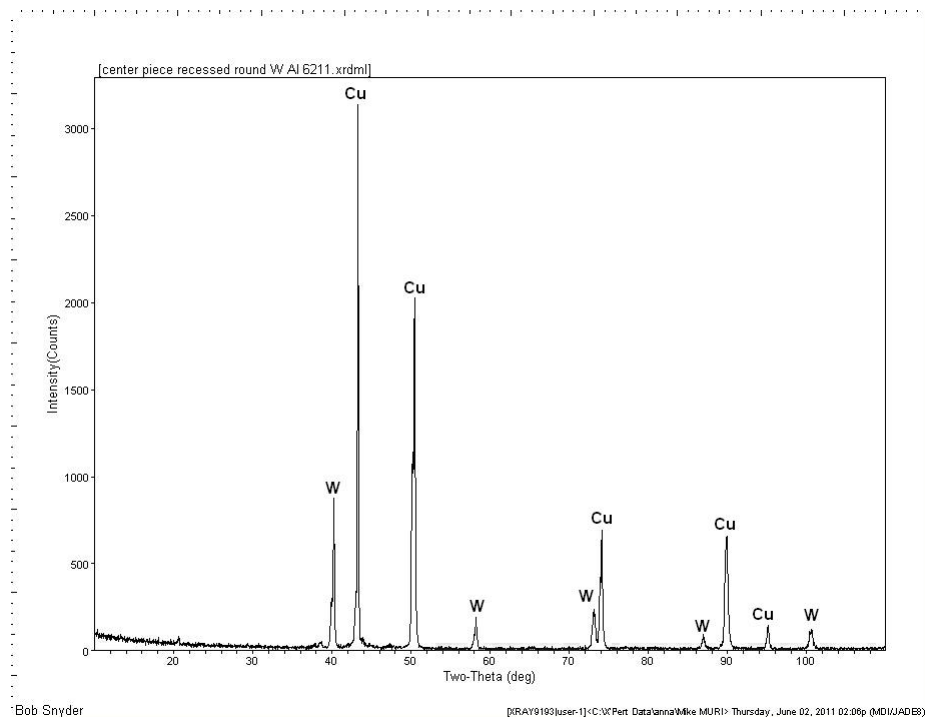


**Figure 53:** XRD trace of repressed projectile packed with equi-volume mix of W+Al fired at maximum velocity  $\approx 480\text{m/s}$  in air

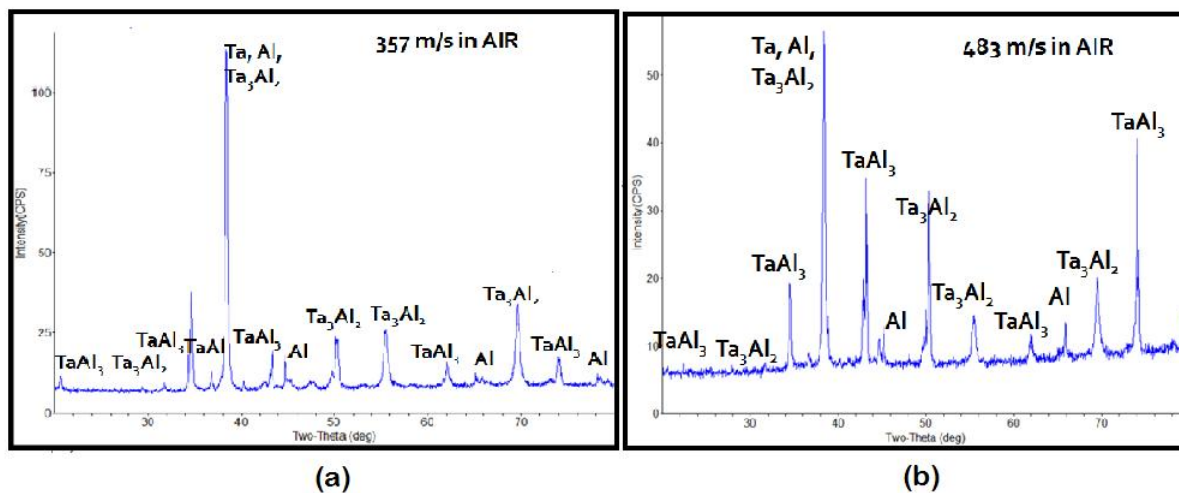


**Figure 54:** XRD trace of material recovered from repressed projectile packed with equi-volume mix of Ta+Al fired at velocities of (a)  $357\text{m/s}$  and (b)  $483\text{m/s}$  in air showing inter-metallic reaction products

## CHAPTER V

### CONCLUSIONS AND FUTURE WORK

#### *5.1 Concluding Remarks*

The purpose of this study was to characterize the impact initiation of Al-based intermetallic-forming reactive materials by determining the reaction initiation threshold in air and vacuum environments. The threshold was based on the total energy for reaction initiation, and was normalized for comparison of the various intermetallic-forming systems, and to evaluate reaction mechanisms based on oxidation or anaerobic processes. The experiments were performed on tantalum-aluminum, tungsten-aluminum, nickel-aluminum, and pure aluminum powder mixture compacts uniaxial stress impact testing in a modified gas gun rod-on-anvil Taylor test.

The velocity of the test samples were recorded and respective total kinetic energy was calculated. The kinetic energy for threshold of reaction initiation in each system of materials for both air and vacuum, was based on conditions in which light emission was recorded. Impact experiments were also used to capture the ejecta, employing recessed projectile and polycarbonate rings. The resulting captured ejecta was subjected to product characterization through X-ray diffraction. While most of the samples yielded inconclusive results, one experimental setup with recessed projectiles on the most reactive sample system of Ta+Al yielded intermetallic products of  $Ta_3Al_2$  and  $TaAl_3$ .

It was observed that Ta+Al and W+Al reacted both in air and vacuum while Ni+Al and Al compacts reacted only in air. Ta+Al is observed to be more reactive due to the mechanical properties of Ta and its relatively high density, which adds energy in the form of heat from strain/flow during localized and bulk deformation of the samples themselves. The reactivity threshold for Ta+Al, in both air and vacuum, was lower than all other systems by 195 kJ (Ta+Al threshold is 718 kJ followed by Al at 913 kJ) in air and 348 kJ (Ta+Al threshold 863 kJ W+Al's is 1211 kJ) in vacuum. From the apparent trends and threshold

data in Figures 38 to 39 and Table 12 respectively, it can be seen in air that Al, W+Al, and Ni+Al (at a higher packing density) all react at about the same threshold close to  $\approx$  1000 kJ, indicating that Al is the main determinant in reaction and that its dominated by its oxidation. Ta+Al compacts however, react at a threshold much lower than that of Al. This, and Ta+Al's ability to react in vacuum, point toward the conclusion that Ta+Al undergoes anaerobic intermetallic reactions, while the other systems are dependent on Al's oxidation.

In the case of Ni+Al, and Ta+Al at relatively constant velocity, packing density effect was manifested as reaction initiation characteristics improved with increasing packing density of the samples. It also can be seen that particle size affects the reactivity of samples and can offset the negative effect of lower to packing density. In evaluating Ni+Al, both -325 mesh and +325 -200 mesh samples showed similar trends of packing density effects. However, the coarser +325 -200 mesh samples were far more reactive resulting in reaction with significantly lower reaction initiation energy than all of -325 mesh Ni+Al samples.

## ***5.2 Recommendations for Future Work***

### **5.2.1 Characterization Techniques**

A different approach should be taken to recover post reaction products. Larger sample sizes should result in more debris for examination as in the case of the recessed projectile that used about three times as much powder in experimentation. This points to the development of modified impact initiation testing by optimizing the recessed projectile design with a cap or slightly recessed lip design to seat machine pressed samples, creating an anvil with a recessed target area to capture reaction products in a confined area, or test with samples of a larger diameter (a .25 inch sample press instead of .125 inch) using a polycarbonate ring to capture ejecta. Using a larger scale experiment in the form of a reverse anvil-on-rod Taylor test, where a recovery fixture can be developed to accelerate a projectile through a 80 mm diameter, 25 foot long barrel into a mounted sample should also increase retention of post reaction products.

To better compare oxidation versus anaerobic reactions, spectroscopy can be used during

the rod-on-anvil testing to determine if at any point the light or spectra given off during a reaction relates to the formation of the oxide or intermetallic process. Other methods to address oxidation could be to perform experiments in an inert backfilled environment where the chamber is evacuated and then purged with Argon to further reduce the oxygen available in the chamber at a time. An oxygen sensor can also be used to note the oxygen level in the experimental chamber. These experiments can be repeated with the oxygen sensor in place, noting levels of oxygen in ambient, evacuated, and backfilled-and-evacuated-Argon conditions for comparison.

A transparent target plate through the use of sapphire can be used. This has the ability to mount fiber optics for spectroscopy and the capability to show both sample deformation from a side and head-on point of view, allowing for the better understanding of how the deformation occurs prior to reaction initiation. This could also be used with an infrared camera to show preferential ignition or reaction initiation sites (hot spots).

### **5.2.2 Material Systems**

Given the packing density effects at a relatively constant velocity for pure Al and the work done by Herbold et al [41], it could be beneficial to investigate an optimum density for reaction, where the reaction thresholds for initiation are compared in multiple environments. Varying the particle size of the intermetallic-forming system for an optimal mix of reactivity as well as increasing the stoichiometric ratio mixture range (1:5, 1:4, 1:3, 3:1, etc. by atomic percent) could determine how much of each part of an intermetallic-forming mixture is necessary to cause a reaction, what ratio provides the most intense light from reaction and what conditions provide desired reaction products, and/or what ratio provides a mix that reacts with the least amount of kinetic energy.



## REFERENCES

- [1] N. Patel, “Intermediate Strain Rate Behavior of Two Structural Energetic Materials,” 2004. 1, 3
- [2] L. Ferranti Jr, “Mechanochemical reactions and strengthening in epoxy-cast aluminum iron-oxide mixtures,” 2007. 1, 3
- [3] B. Aydelotte and N. Thadhani, “Impact initiated reaction of explosively compacted binary powder mixtures,” 2011. 1, 56
- [4] D. Eakins and N. Thadhani, “Instrumented taylor anvil-on-rod impact tests for validating applicability of standard strength models to transient deformation states,” *Journal of Applied Physics*, vol. 100, no. 7, 2006. 2
- [5] A. C. Whiffin, “The use of flat-ended projectiles for determining dynamic yield stress. II. tests on various metallic materials,” *Proceedings of the Royal Society of London. Series A, Mathematical and Physical Sciences*, vol. 194, no. 1038, p. 300322, 1948. 2
- [6] S. W. Du and N. N. Thadhani, “Impact initiation of pressed al-based intermetallic-forming powder mixture compacts,” *AIP Conference Proceedings*, vol. 1195, no. 1, pp. 470–473, 2009. 2
- [7] S. Walley, J. Balzer, W. Proud, and J. Field, “Response of thermites to dynamic high pressure and shear,” *Proceedings of the Royal Society of London. Series A: Mathematical, Physical and Engineering Sciences*, vol. 456, no. 1998, p. 1483, 2000. 3, 13, 14, 16
- [8] *A Survey of Combustible Metals Thermites and Intermetallics for Pyrotechnic Applications*, 1996. 3, 5, 31

- [9] S. Umbrajkar, C. Chen, M. Schoenitz, and E. Dreizin, “On problems of isoconversion data processing for reactions in Al-rich Al-MoO<sub>3</sub> thermites,” *Thermochimica Acta*, vol. 477, no. 1-2, pp. 1–6, 2008. 6, 9, 10
- [10] S. Umbrajkar and E. Dreizin, “Kinetic Analysis of Thermite Reactions in Al–MoO<sub>3</sub> Nanocomposites,” *Journal of Propulsion and Power*, vol. 23, no. 4, p. 683, 2007. 6, 8
- [11] E. Shafirovich, A. Mukasyan, L. Thiers, A. Varma, B. Legrand, C. Chauveau, and I. Gokalp, “Ignition and combustion of Al particles clad by Ni,” *Combustion science and technology*, vol. 174, no. 3, pp. 125–140, 2002. 6, 11
- [12] Y. Shoshin, M. Trunov, X. Zhu, M. Schoenitz, and E. Dreizin, “Ignition of aluminum-rich Al-Ti mechanical alloys in air,” *Combustion and flame*, vol. 144, no. 4, pp. 688–697, 2006. 6, 7, 8
- [13] S. Spey Jr, *Ignition properties of multilayer nanoscale reactive foils and the properties of metal-ceramic joints made with the same*. PhD thesis, John Hopkins University, 2005. 6, 7, 17, 52
- [14] S. Umbrajkar, M. Schoenitz, and E. Dreizin, “Exothermic reactions in Al-CuO nanocomposites,” *Thermochimica acta*, vol. 451, no. 1-2, pp. 34–43, 2006. 8
- [15] H. Kissinger, “Reaction kinetics in differential thermal analysis,” *Analytical chemistry*, vol. 29, no. 11, pp. 1702–1706, 1957. 9
- [16] Z. Zhang, D. Fouchard, and J. Rea, “Differential scanning calorimetry material studies: implications for the safety of lithium-ion cells,” *Journal of power sources*, vol. 70, no. 1, pp. 16–20, 1998. 9, 10
- [17] B. Legrand, E. Shafirovich, M. Marion, C. Chauveau, and I. Gokalp, “Ignition and combustion of levitated magnesium particles in carbon dioxide,” vol. 27, no. 2, pp. 2413–2419, 1998. 11, 12

- [18] G. Taylor, “The use of flat-ended projectiles for determining dynamic yield stress. i. theoretical considerations,” *Proceedings of the Royal Society of London. Series A, Mathematical and Physical Sciences*, vol. 194, no. 1038, p. 289299, 1948. 18
- [19] K. L. Torres, H. A. Clements, S. E. Jones, M. Dilmore, and B. Martin, “Dynamic strength estimates for a high-strength experimental steel,” *Journal of Pressure Vessel Technology*, vol. 131, no. 2, p. 021404, 2009. 18, 19
- [20] R. G. Ames, “Energy release characteristics of impact-initiated energetic materials,” *MATERIALS RESEARCH SOCIETY SYMPOSIUM PROCEEDINGS*, 2006. 18, 20, 21, 22, 23, 24, 25
- [21] J. Gilman, “Direct Evidence of Chemical Reactions Induced by Shear-Strains,” in *MATERIALS RESEARCH SOCIETY SYMPOSIUM PROCEEDINGS*, vol. 800, pp. 287–298, Warrendale, Pa.; Materials Research Society; 1999, 2004. 25
- [22] R. Graham, *Solids Under High Pressure Shock Compression: Mechanics, Physics, and Chemistry*. Springer-Verlag, 1992. 25
- [23] E. Teller, “On the speed of reactions at high pressures,” *The Journal of Chemical Physics*, vol. 36, no. 4, pp. 901–903, 1962. 25
- [24] L. V. Al’Tshuler, “Phase transitions in shock waves (review),” *Journal of Applied Mechanics and Technical Physics*, vol. 19, no. 4, p. 496505, 1978. 25
- [25] N. M. A. B. N.-N. W. DC., *Shock Compression Chemistry in Materials Synthesis and Processing*. Defense Technical Information Center, 1984. 25
- [26] R. Graham, B. Morosin, E. Venturini, and M. Carr, “Materials modification and synthesis under high pressure shock compression,” *Annual Review of Materials Science*, vol. 16, no. 1, pp. 315–341, 1986. 25
- [27] N. N. Thadhani, “Shock-induced chemical reactions and synthesis of materials,” *Progress in Materials Science*, vol. 37, no. 2, pp. 117–226, 1993. 25

- [28] I. D. T. I. L.V. Al'tshuler, I. M. Brakalov and P. Yampol'skii *High Energy Chemistry*, 1968. 25
- [29] W. W. J. G. R. Armstrong, N.N. Thadhani and R. Simpson, "Synthesis, characterization and properties of energetic/reactive nanomaterials." Proc. Materials Research Society Symposium, Fall Meet. Boston, MA, USA, December 2003, MRS, 392, 2003. 25
- [30] A. Dremin and O. Breusov, "Processes Occurring in Solids Under the Action of Powerful Shock Waves," *Russian Chemical Reviews*, vol. 37, no. 5, pp. 392–402, 1968. 25
- [31] S. Batsanov, G. Doronin, E. Moroz, I. Ovsyannikova, and O. Ryabinina, "Effect of an explosion on matter formation of solid solutions of rubidium and cesium chlorides," *Combustion, Explosion, and Shock Waves*, vol. 5, no. 2, pp. 193–195, 1969. 25
- [32] N. Thadhani, "Shock-induced and shock-assisted solid-state chemical reactions in powder mixtures," *Journal of Applied Physics*, vol. 76, no. 4, pp. 2129–2138, 2009. 25
- [33] D. Eakins and N. Thadhani, "Shock-induced reaction in a flake nickel+ spherical aluminum powder mixture," *Journal of applied physics*, vol. 100, no. 11, pp. 113521–113521, 2006. 26, 27
- [34] N. Thadhani, R. Graham, T. Royal, E. Dunbar, M. Anderson, and G. Holman, "Shock-induced chemical reactions in titanium–silicon powder mixtures of different morphologies: Time-resolved pressure measurements and materials analysis," *Journal of applied physics*, vol. 82, p. 1113, 1997. 28
- [35] D. Anthony Fredenburg, N. Thadhani, and T. Vogler, "Shock consolidation of nanocrystalline 6061-t6 aluminum powders," *Materials Science and Engineering: A*, vol. 527, no. 15, pp. 3349–3357, 2010. 27
- [36] D. Eakins and N. Thadhani, "Shock compression of reactive powder mixtures," *International Materials Reviews*, 2009. 27

- [37] I. Song and N. Thadhani, “Shock-induced chemical reactions and synthesis of nickel aluminides,” *Metallurgical and Materials Transactions A*, vol. 23, no. 1, pp. 41–48, 1992. 28
- [38] B. Aydelotte, *FRAGMENTATION AND REACTION OF STRUCTURAL ENERGETIC MATERIALS*. PhD thesis, Georgia Institute of Technology, 2010. 31
- [39] *Metals Handbook*, vol. 2. 31
- [40] A. Wolfenden, “Dynamic elastic modulus measurements in materials,” *ASTM International*, 1990. 31
- [41] E. Herbold, N. Thadhani, and J. Jordan, “Observation of a minimum reaction initiation threshold in ball-milled ni+ al under high-rate mechanical loading,” *Journal of Applied Physics*, vol. 109, p. 066108, 2011. 49, 54, 55, 66